

# Antimicrobial Peptides Share a Common Interaction Driven by Membrane Line Tension Reduction

J. Michael Henderson,<sup>1,2,3</sup> Alan J. Waring,<sup>4,5</sup> Frances Separovic,<sup>6</sup> and Ka Yee C. Lee<sup>1,2,3,\*</sup>

<sup>1</sup>Department of Chemistry, <sup>2</sup>Institute for Biophysical Dynamics, and <sup>3</sup>The James Frank Institute, The University of Chicago, Chicago, Illinois; <sup>4</sup>Los Angeles Biomedical Research Institute, Harbor-UCLA Medical Center, Torrance, California; <sup>5</sup>Department of Medicine, David Geffen School of Medicine, University of California, Los Angeles, Los Angeles, California; and <sup>6</sup>School of Chemistry, Bio21 Institute, University of Melbourne, Melbourne, Victoria, Australia

**ABSTRACT** Antimicrobial peptides (AMPs) are a class of host-defense molecules that neutralize a broad range of pathogens. Their membrane-permeabilizing behavior has been commonly attributed to the formation of pores; however, with the continuing discovery of AMPs, many are uncharacterized and their exact mechanism remains unknown. Using atomic force microscopy, we previously characterized the disruption of model membranes by protegrin-1 (PG-1), a cationic AMP from pig leukocytes. When incubated with zwitterionic membranes of dimyristoylphosphocholine, PG-1 first induced edge instability at low concentrations, then porous defects at intermediate concentrations, and finally worm-like micelle structures at high concentrations. These rich structural changes suggested that pore formation constitutes only an intermediate state along the route of PG-1's membrane disruption process. The formation of these structures could be best understood by using a mesophase framework of a binary mixture of lipids and peptides, where PG-1 acts as a line-active agent in lowering interfacial bilayer tensions. We have proposed that rather than being static pore formers, AMPs share a common ability to lower interfacial tensions that promote membrane transformations. In a study of 13 different AMPs, we found that peptide line-active behavior was not driven by the overall charge, and instead was correlated with their adoption of imperfect secondary structures. These peptide structures commonly positioned charged residues near the membrane interface to promote deformation favorable for their incorporation into the membrane. Uniquely, the data showed that barrel-stave-forming peptides such as alamethicin are not line-active, and that the seemingly disparate models of toroidal pores and carpet activity are actually related. We speculate that this interplay between peptide structure and the distribution of polar residues in relation to the membrane governs AMP line activity in general and represents a novel, to our knowledge, avenue for the rational design of new drugs.

## INTRODUCTION

With the overuse and misuse of antibiotics, pathogens that were once highly susceptible to treatment have acquired multidrug resistance, leading to escalating hospitalizations and healthcare costs (1). Host-defense peptides, commonly known as antimicrobial peptides (AMPs), are a potential solution to this crisis. Serving as a first line of defense against infections, AMPs are small, predominantly cationic, amphipathic peptides that are found ubiquitously in the innate (i.e., nonspecific) immune response of living organisms (2,3). Their localization to vulnerable tissues ensures that they can rapidly neutralize a broad range of microorganisms, including bacteria, fungi, and even viruses. Unlike conventional antibiotics, which interfere with easily mutable targets (e.g., cell wall construction, protein biosyn-

thesis, and genetic material replication), AMPs are believed to target the more evolutionarily stable cell membranes of invading pathogens by disrupting their barrier function to cause eventual cell death. The membrane-permeabilizing activity of AMPs is an advantageous characteristic in the design of new drugs; however, the general mechanism by which this activity occurs remains poorly understood and contested, limiting their potential clinical application.

It has long been suggested that membrane-active AMPs induce membrane pores (4–7), with the pore structure conforming to either the barrel-stave or toroidal type (8,9). For example, alamethicin (ALM) (4,9,10) and pardaxin (6,11) are thought to form barrel-stave pores in which the peptide monomers form tight cylindrical bundles, whereas AMPs such as protegrin-1 (12,13), magainin (7,12), human defensins (14), and frog caerins (15) form toroidal pores with curved peptide-lipid edges. However, direct observation to differentiate between these pore types for an AMP is difficult and largely limited to intensive x-ray and neutron

Submitted July 7, 2016, and accepted for publication October 5, 2016.

\*Correspondence: [kayeelee@uchicago.edu](mailto:kayeelee@uchicago.edu)

Editor: Paulo Almeida.

<http://dx.doi.org/10.1016/j.bpj.2016.10.003>

© 2016 Biophysical Society.

scattering methods (8,9,12). Unlike AMPs that form pores of a well-defined size, AMPs that disrupt cell membranes through a nonpore mechanism, known as the carpet model, accumulate on the membrane surface and remain interfacially in contact with the lipid headgroups throughout the process of membrane destabilization, never inserting to span the bilayer in an organized fashion. Although it was originally proposed to describe the action of dermaseptin (16), an amphipathic  $\alpha$ -helix rich in Lys that resembles magainin, the carpet model has been referenced to explain the activity of AMPs that are too short to span the entire bilayer (e.g., aurein and citropin) and thus are needed in higher concentrations to elicit membrane permeation (15,17,18).

With more than 1000 AMPs discovered to date (19), it is evident that these peptides vary widely in their primary sequences and adopt all kinds of secondary structures, including random linear,  $\alpha$ -helical, and  $\beta$ -sheet motifs. This variety has prompted the development of a number of models to explain observations from the many techniques that have been used to investigate AMP interactions (20,21). Relatively few AMPs have been thoroughly investigated; however, it would be a daunting task to categorize the activity of each AMP into a prevailing pore or nonpore model. Although sequence homology has been implicated in eliciting AMP membrane activity (22), the diversity of AMPs across species challenges our ability to predict key structure-function relationships when designing novel drugs. For this reason, attempts to achieve rational peptide design remain rare and have principally identified positive charge and amphiphilicity as key properties for AMP activity. These properties have encouraged the development of novel polymeric mimics that display selective antimicrobial activity across a variety of ordered and nonordered structures (3). Evolutionarily speaking, it would be costly (and thus unlikely) for each peptide to adopt its own membrane-disruption mechanism. Peptide plasticity would offer a clear evolutionary advantage in terms of both sequence and structure, allowing AMPs to utilize a single underlying mechanism in interacting with the membranes of various pathogens. If such a universal mechanism exists, we could improve the rational design of new antimicrobial agents by gaining a better understanding of the underlying physicochemical properties that govern a shared AMP mechanism.

We recently showed that the disruption of supported lipid bilayers by protegrin-1 (PG-1), an 18-residue, cationic,  $\beta$ -sheet AMP isolated from pig leukocytes, proceeded in a concentration-dependent manner (23,24). The insertion of PG-1 into zwitterionic 1,2-dimyristoyl-*sn*-glycero-3-phosphocholine (DMPC) bilayers resulted in membrane structural transformations that extended beyond simple pores and included instabilities at the bilayer edge and the presence of worm-like micelles at higher peptide concentrations. The spectrum of self-assembled structures showed that PG-1 acts to lower the interfacial line energy of the bilayer in a manner similar to that exhibited by amphiphilic

detergents, which are capable of generating and stabilizing normally unfavorable line geometries (i.e., curved edges) in membranes. Classifying PG-1's mechanism as a static pore former does not account for the full structural transformations we observed. Instead, PG-1's activity should be reframed as a dynamic transition between different self-assembled structures that depends on the relative ratio between peptide and lipid. To this end, we have proposed that AMPs in general share this line-active behavior and act universally in a detergent-like manner.

In this work, we used atomic force microscopy (AFM) to image the structural transformations of supported DMPC bilayer patches induced by different AMPs (listed in Table S1 of the Supporting Material). The investigated AMPs are broadly active against many pathogens (see Table S2 for representative minimum inhibitory concentrations (MICs) against common pathogenic bacteria) and vary considerably in their secondary structures (Figs. S1–S4). By deliberately using a zwitterionic lipid rather than one with a charged headgroup, we were able to better identify other membrane attributes that dictate AMP interactions. We show that with the exception of ALM, the activity of the investigated peptides is driven by a common physical principle that reduces membrane line tension. Our findings indicate that line-active behavior is not dependent on the peptide charge, and we suggest instead that the activity originates from imperfect amphipathic structures, which usually position charged Lys and Arg residues at the bilayer interfaces to promote the creation of line geometries within the membrane. These line geometries facilitate binding of the peptides to the edge, which raises the peptide/lipid (P/L) ratio and structurally transforms the lamellar bilayer into micelles. Our results show that any barrel-stave-forming peptide would not be line-active, and that seemingly disparate peptides categorized into either the toroidal-pore or carpet model are actually related through this line-active model of AMP interaction.

## MATERIALS AND METHODS

### Materials

Chemical reagents (certified ACS or BioReagent grade, purity  $\geq 99\%$ ) and high-performance liquid chromatography-grade organic solvents were purchased from Fisher Scientific (Waltham, MA). Powder DMPC was purchased from Avanti Polar Lipids (Alabaster, AL) and used without further purification. ALM was obtained as a 5 mg/mL stock solution in DMSO from Sigma-Aldrich (St. Louis, MO). Custom synthesis of aurein-1.1, dermaseptin-1, human  $\beta$ -defensin-1, histatin-2, indolicidin, and magainin-1 was done by Anaspec (Fremont, CA), and synthesis of caerin-1.3, citropin-1.1, kalata-B3, and pardaxin-1 was performed by bioWORLD (Dublin, OH). PG-1 synthesis was conducted in house and has been thoroughly described elsewhere (13). Peptide purity was assessed by high-performance liquid chromatography and determined to be  $\geq 95\%$  by peak area analysis. All aqueous solutions were prepared with ultrapure water (resistivity  $>18 \text{ M}\Omega\cdot\text{cm}$ ) from a Milli-Q Advantage A-10 purification system (EMD Millipore, Billerica, MA). Peptide stocks were prepared and quantified as described in Supporting Materials and Methods.

## Membrane-disruption assay

Details concerning the preparation of large unilamellar vesicles (LUVs) and solid-supported phospholipid bilayers (SPBs) on mica are provided in [Supporting Materials and Methods](#) along with descriptions of the image acquisition, processing, and analysis. Briefly, DMPC SPB patches were imaged under buffer by tapping-mode AFM at 30°C before and after the addition of peptide. SPB patches were used instead of a contiguous membrane because the latter does not permit membrane expansion upon peptide insertion, and only increased membrane roughness has been reported for pore-forming AMPs such as PG-1 (25). The peptide was equilibrated with the bilayers for at least 15 min, after which structural changes of the same SPB patch were monitored. This protocol was repeated by sequentially adding increasing bulk peptide concentrations. During equilibration, the free peptides in the bulk adsorbed to the membranes until a surface partition equilibrium was achieved, resulting in the P/L being directly proportional to the bulk peptide concentration.

## RESULTS AND DISCUSSION

### Peptide line activity induces membrane structural transformations beyond pores

We recently demonstrated a detergent-like behavior of PG-1 (23,24) that induces membrane disruption through a range of structural transformations beyond pore formation. The structural transformations induced by PG-1 serve as a reference in the study presented here, which focuses on AMP line activity in general. We performed new image analysis in this study to calculate a bilayer shape factor ( $S$ ) that is used to illustrate contrasting behavior between line-active and nonline-active peptides. In the absence of

peptide (Fig. 1 A), the SPB patches were nearly round, with an average shape factor of  $S = 1.33 \pm 0.17$  (standard deviation (SD),  $n = 100$ ) and displayed smooth edges from a high interfacial line tension. The average membrane thickness was  $4.7 \pm 0.7$  nm (SD,  $n = 45$ ), which is within error of our previous value (23,24) and comparable to neutron scattering results obtained for DMPC SPBs and LUVs (26,27). To prevent hydrophobic core exposure to the aqueous environment, lipids self-assemble at the edge to form a seamlessly curved cap (28). As lipids have an innate curvature, edge alignment causes clashing of the acyl chains and induces steric stress within this confining geometry. A penalty is exacted to maintain lipids in this less favorable state and manifests as a line energy, a one-dimensional (1D) equivalent of the familiar two-dimensional (2D) surface energy. The line tension then acts to minimize the overall energy of the system by reducing the ratio of bilayer perimeter length to surface area. The equilibrium size of an SPB patch is therefore determined by the balance of two forces: the line tension, which favors compact shapes, and a repulsive interaction from the phospholipid dipoles, which favors extended boundaries (29). Line-active agents (e.g., amphiphilic detergents) can adsorb to an exposed edge, reducing the line tension and stabilizing extended line geometries (e.g., curved edges like those of pores) (30–34). The presence of a line geometry provides a metric for assessing AMP line activity, although a bilayer edge is initially absent in vivo when an AMP encounters a target membrane.

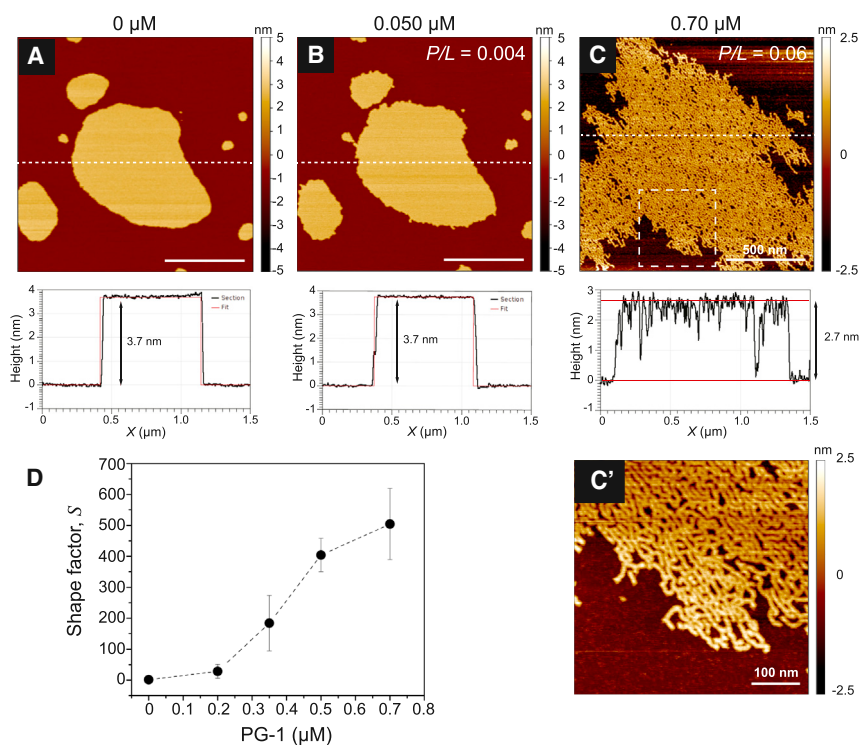


**FIGURE 1** DMPC membrane structural transformations induced by PG-1's line-active behavior. (A) In the absence of PG-1, the bilayer was compact and nearly circular with a smooth and minimized edge. (B) Introduction of 0.050  $\mu$ M PG-1 caused the bilayer to extend and become roughened, and this remained stable over time. Line sections (dashed white lines) of the bilayer before and after the introduction of 0.050  $\mu$ M PG-1 showed that the lamellar core remained unaffected, and that PG-1 adsorption at the curved edge resulted in a reduction in the bilayer line tension. (C) With increasing bulk PG-1 concentrations, the lamellar organization of the bilayer was compromised by 0.70  $\mu$ M PG-1, with the formation of worm-like micelles. Peptide insertion thinned the membrane considerably (by  $\sim 1$  nm). To better reveal the bilayer's transformation in (C), the height data were rescaled to a 5 nm range. The dashed box in (C) indicates a zoomed-in region ( $500 \times 500$  nm<sup>2</sup>) that is shown in (C'). (D) A shape factor analysis of the bilayer morphology ( $S$ ) as a function of the bulk PG-1 concentration showed that PG-1 had a considerable effect in promoting extended morphologies with increased perimeter lengths beyond initial values near  $S = 1$ . Error bars in (D) are SDs from at least three replicate bilayer monitoring experiments. All images were obtained at 30°C. White scale bars are 500 nm unless otherwise indicated. To see this figure in color, go online.

As shown in Fig. 1 B, a low concentration of PG-1 (0.050  $\mu\text{M}$ ) caused the bilayer boundary to extend and become destabilized from its once smooth contour, whereas the bilayer core remained undisturbed with no discernible pore formation. Line sections confirmed that the bilayer center remained flat and did not alter in thickness with the addition of PG-1. The calculated shape factor increased from an initial, nearly circular value ( $S \approx 1$ ) to  $S = 1.94$ , confirming that an extended boundary had resulted from the presence of peptides. This suggested that the curved bilayer edge was more susceptible to initial PG-1 binding as compared with the lamellar region of the bilayer patch, as the line sections revealed no discernible membrane height change. The stability of the extended morphology resulted from an apparent reduction in the line tension caused by PG-1's line-active behavior. Indeed, recent molecular dynamics (MD) simulations have shown that PG-1 readily adsorbs to curved edges (35) and lowers line tensions in a concentration-dependent manner (24).

PG-1 interaction within the bilayer core also caused remodeling of the membrane structure. New edges were created within the patch, presumably from the initial formation of toroidal pores, which facilitated favorable binding of more PG-1, further lowering the line tension and allowing porous defects to grow to an observable size (Fig. S5 A). This edge extension allowed for yet more binding of PG-1 and ever-expanding porous defects (Fig. S5, B and C), culminating in the complete structural transformation of the lamellar bilayer into a network of worm-like micelles by 0.70  $\mu\text{M}$  PG-1 (Fig. 1 C). The rise of  $S$  as a function of bulk PG-1 concentration (Fig. 1 D) revealed a considerable expansion of the bilayer boundary and demonstrated the accelerating loss of membrane integrity that coincided with PG-1's line-active behavior. A relative height change between the data in Fig. 1, A and C, showed a thinning of nearly 27%. This agrees with the work by Huang and co-workers in which they established a relationship between

the insertion state of AMPs and the degree of elastic membrane deformation by showing that various AMPs, including ALM (36), magainin-2 (37), and PG-1 (38), caused membrane thinning in direct proportion to the peptide concentration. The lipid-peptide self-assembled structures that formed were identical to those that formed between bilayer-forming lipids and amphiphilic detergents such as the short-chain lipid dihexanoylphosphatidylcholine (39) and sodium cholate (40). The variety of structural transformations observed in these studies shows that PG-1's antimicrobial activity is similar to the behavior of a detergent adsorbing to an interface, in the manner of a Gibbs adsorption isotherm (32). Therefore, we propose that membrane-active AMPs act universally within a detergent-like framework in which pore formation is not the defining mechanism but instead represents a small part of a complex process that encompasses lipid-peptide aggregates in addition to lamellar bilayers.

### Barrel-stave-forming peptides exhibit nonlinear-active behavior

For comparison with PG-1's line-active behavior, we assessed the interaction of another common pore-forming AMP, ALM, whose barrel-stave pore has been well characterized. Fig. S1 contrasts the secondary structure of ALM with that of PG-1, showing that ALM achieves an ideal, amphipathic helix, whereas PG-1 lacks discrete, separated faces of hydrophilic and hydrophobic residues. The concentration-dependent interaction of ALM with DMPC bilayers is shown in Fig. 2. As the ALM concentration increased, the bilayer patches in Fig. 2 A expanded and fused upon contact (Fig. 2 B) to result in a single bilayer patch by 25  $\mu\text{M}$  (Fig. 2 C) that continued to grow laterally (Fig. 2 D). A control injection mimicking that of 50  $\mu\text{M}$  ALM (Fig. S6) showed no large-scale membrane expansion and ruled out possible effects from the traces of DMSO and methanol

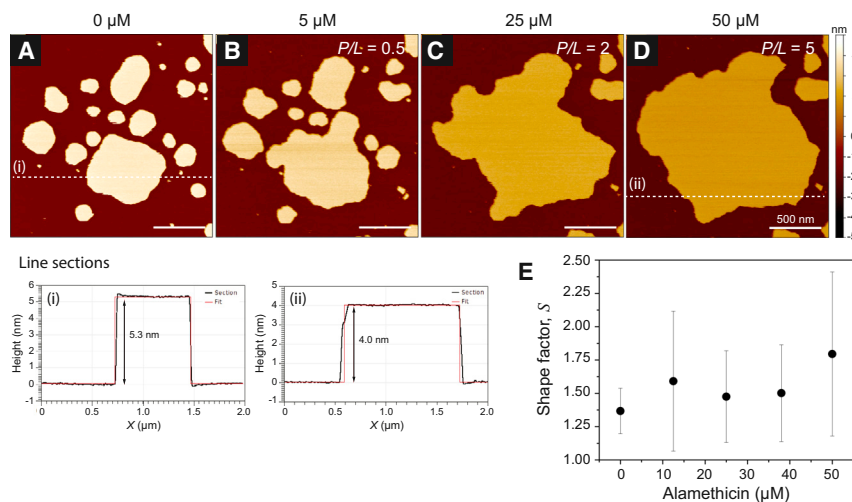


FIGURE 2 Concentration-dependent interaction of ALM with DMPC bilayer patches. (A) The unperturbed bilayer patches in the absence of ALM displayed smooth edges and compact shapes, as shown in Fig. 1 A. (B–D) Through the course of successive injections, the concentration of ALM was raised from 5  $\mu\text{M}$  (B) to 25  $\mu\text{M}$  (C) and finally to 50  $\mu\text{M}$  (D). In contrast to the structural transformations induced by PG-1, ALM had a negligible effect on the bilayer morphology and instead only caused gross lateral expansion of the bilayers. Line sections (dashed white lines) revealed progressive membrane thinning, presumably from peptide insertion, although pores were not observed. (E) Shape factor analysis as a function of increasing ALM concentration. Error bars in (E) are SDs from five replicate bilayer monitoring experiments to confirm repeatability. All images were obtained at 30°C. White scale bars are 500 nm. To see this figure in color, go online.



present in the ALM stock. Assuming lipid conservation between injections, membrane expansion coincides with peptide insertion as additional molecules are progressively added. When a peptide partitions to the bilayer, the lipid acyl chain volume remains constant; therefore, the expansion coincides with a decrease in the membrane thickness (41). From a comparison of the micrographs in Fig. 2, it is evident that the membrane thinned in a concentration-dependent manner, and a line section analysis showed that by 50  $\mu\text{M}$  (Fig. 2 D) the membrane was relatively thinner (by 25%). As with PG-1, membrane thinning is an indication of peptide insertion and is a documented trait of ALM's interaction with membranes (36).

Pores were not detectable via AFM imaging, as the diameter of the ALM pore was smaller than the quoted tip radius of 8 nm and thus too small to resolve. Using a calcein-leakage assay (see [Supporting Materials and Methods](#)), we confirmed ALM-induced pore formation in our DMPC bilayer system, which contributed to the bilayer expansion observed in Fig. 2. The degree of ALM-induced leakage (shown in Fig. S7 A) was greater than the background leakage of dye-loaded DMPC vesicles alone. The fraction of released dye and the apparent rate,  $k_{app}$ , of the efflux (Fig. S7 B) increased in a concentration-dependent manner, eventually reaching complete leakage. The leakage profiles fit well to a double-exponential decay function, from which we extract the rates of contributing processes, including pore formation. In a double-exponential model, the overall leakage profile must be a combination of at least two simultaneous kinetic processes. As previously described for several membrane-active peptides and polymers, the leakage mechanism is assumed to involve one kinetic process at a rate of  $k_1$ , which causes only transient leakage and approaches a finite value over time, and a second process at a rate of  $k_2$ , which causes unlimited leakage through stable pore formation (42–44). At the low concentration of 0.05  $\mu\text{M}$  ALM, the leakage profile (Fig. S7 A) reached a maximum leakage near 70% and thus was dominated more by the transient leakage process. As the ALM concentration increased, the second process began to dominate and ultimately led to complete vesicle leakage. Fig. S7 C shows the amplitude of the second leakage process as a function of the rate constant  $k_2$ . ALM-induced pore formation dominated the leakage profile as the concentration increased, since the probability of pore formation must increase in a concentration-dependent manner. Although ALM pores were too small to visualize by AFM, they were present at the higher concentrations shown in Fig. 2 and thus contributed to the observed bilayer expansion. The interaction was devoid of the membrane structural transformation seen with PG-1 (Figs. 1 and S5). Dynamic light scattering (Fig. S8) showed that the addition of ALM did not disrupt the dye-loaded LUVs, as only single peaks were obtained, indicating intact vesicles with a homogeneous size distribution. An increase in the LUV diameter from 122 to 173 nm occurred at

a P/L ratio of  $\sim 0.3$  (50  $\mu\text{M}$  ALM) and corroborates the onset of membrane expansion observed in the AFM measurements at a similar P/L ratio (Fig. 2 B).

Fig. 2 E shows the bilayer shape factor as a function of ALM concentration, averaged across several experiments. The shape factor remained invariant with increasing concentrations, indicating that ALM's insertion had no pronounced effect on the promotion and stabilization of extended bilayer morphologies. This trend is contrary to the case with PG-1 (Fig. 1 D), where a persistent change in bilayer morphology indicated a considerable expansion of the bilayer boundary, supporting the line-active behavior of PG-1. We conclude that ALM interacts with the membranes in a nonline-active way. This conclusion is supported by the different pore structure formed by ALM compared with PG-1. In the barrel-stave configuration, ALM monomers tightly associate to form a cylindrical pore without a curved edge as a result of their high hydrophobicity and lack of charged residues along the helix. The hydrophobic face of the ALM helix, to a first approximation, assumes the shape of a wedge, and thus only a finite number of peptide monomers can favorably associate to create such a tight circular bundle. This constraint on the aggregate size of the pore places an upper limit on the size to which an ALM pore can grow. Consequently, ALM does not favorably permit bilayer edge growth, which explains the invariant shape factor trend (Fig. 2 E) and the retention of bilayer integrity seen in both AFM (see Fig. 2) and dynamic light scattering (see Fig. S8) measurements across a large concentration range. In contrast, the greater polarity of PG-1 necessitates peptide spacing along an edge with lipid headgroups dispersed in between. These lipids in turn must curve from one leaflet to the other to accommodate the polar and apolar regions of the peptide. Toroidal pores can vary in size and grow in diameter as more peptides bind to the edge. In the case of PG-1, this behavior resulted in the growth of defects to the extent that the bilayer was structurally transformed into worm-like micelles.

Recent simulations have shown that many AMPs bind more strongly to curved membrane edges (24,35,45,46). Using nanoscopic secondary ion mass spectrometry imaging, Rakowska et al. (47) showed that the peptide amhelin was enriched at the membrane edge and could induce the growth of unusually large defects, several microns in diameter. The contrasting results for PG-1 and ALM suggest that line activity may depend on the overall charge of the peptide and an interplay between hydrophilic and hydrophobic residues. To address this issue, we tested 11 other peptides (listed in Table S1) that differed in charge and amphipathic secondary structures to ascertain their line-active ability.

### The concentration response of line activity is invariant with peptide charge

Within a line-active model for AMP behavior, we assume that peptides with increasing charge, either positive or

negative, should be more disruptive than neutral peptides. The size of a bilayer patch is determined by a balance between the opposing forces of line tension and electrostatic repulsion. Peptide adsorption charges the membrane, intensifying the electrostatic repulsion, and when this is coupled with line-active behavior, the compact shape of the bilayer becomes unstable and displays extended morphologies. In effect, the instabilities observed in these 2D membranes are related to the more common 3D case of the Rayleigh effect, which describes shape instabilities in spherical drops of increasing charge.

Figs. 3, 4, and 5 show the concentration-dependent interactions of charged and neutral AMPs. Most AMPs are predominantly cationic, and this characteristic has long been used as a simple electrostatic argument for AMP selectivity toward pathogens, as prokaryotic membranes are largely negatively charged and mammalian membranes are largely zwitterionic. Fig. 3 shows that the positively charged peptides aurein-1.1 (Fig. 3 A), citropin-1.1 (Fig. 3 B), magainin-1 (Fig. 3 C), dermaseptin-1 (Fig. 3 D), indolicidin (Fig. 3 E), and human  $\beta$ -defensin-1 (HBD-1) (Fig. 3 F) clearly display line activity that causes the membrane to undergo structural transformations similar to those observed

with PG-1. The line-active behavior of the cationic peptides is most notable in Fig. 3, A2, B2, C2, D2, E2, and F2, which show edge instability at low peptide concentrations. We observe that AMPs that are thought to interact only according to the carpet model (e.g., aurein-1.1, citropin-1.1, and dermaseptin-1) result in the same final micellized state as peptides that insert into and span the membrane, forming a transmembrane pore (e.g., PG-1, magainin-1, indolicidin, and HBD-1). This suggests that these two models share an underlying ability to lower line tension that drives peptide-induced membrane transformations. Moreover, we show that this commonality extends to negatively charged (Fig. 4) and neutral (Fig. 5) AMPs.

Distinct from the majority of cationic AMPs, dermcidin (DCD), a flexible peptide from human sweat that bears a helix-hinge-helix motif (48,49), and kalata-B3 (KB3), a plant cyclotide that displays a knotted topology of three disulfide bridges (50), are AMPs with net negative charges at physiological pH, and represent important exceptions to the prevailing electrostatic model of AMP selectivity. Both DCD and KB3 are broadly active against many prokaryotic pathogens despite having noncanonical negative charges (48,51), and are speculated to form multimeric pores

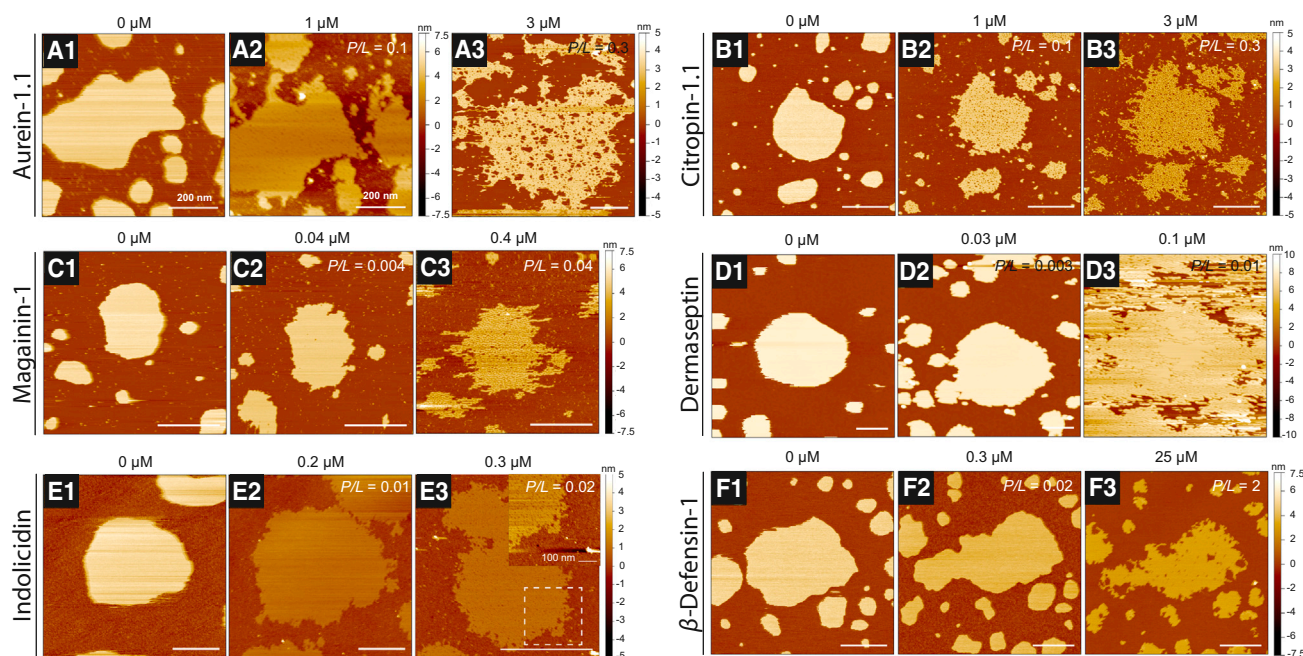
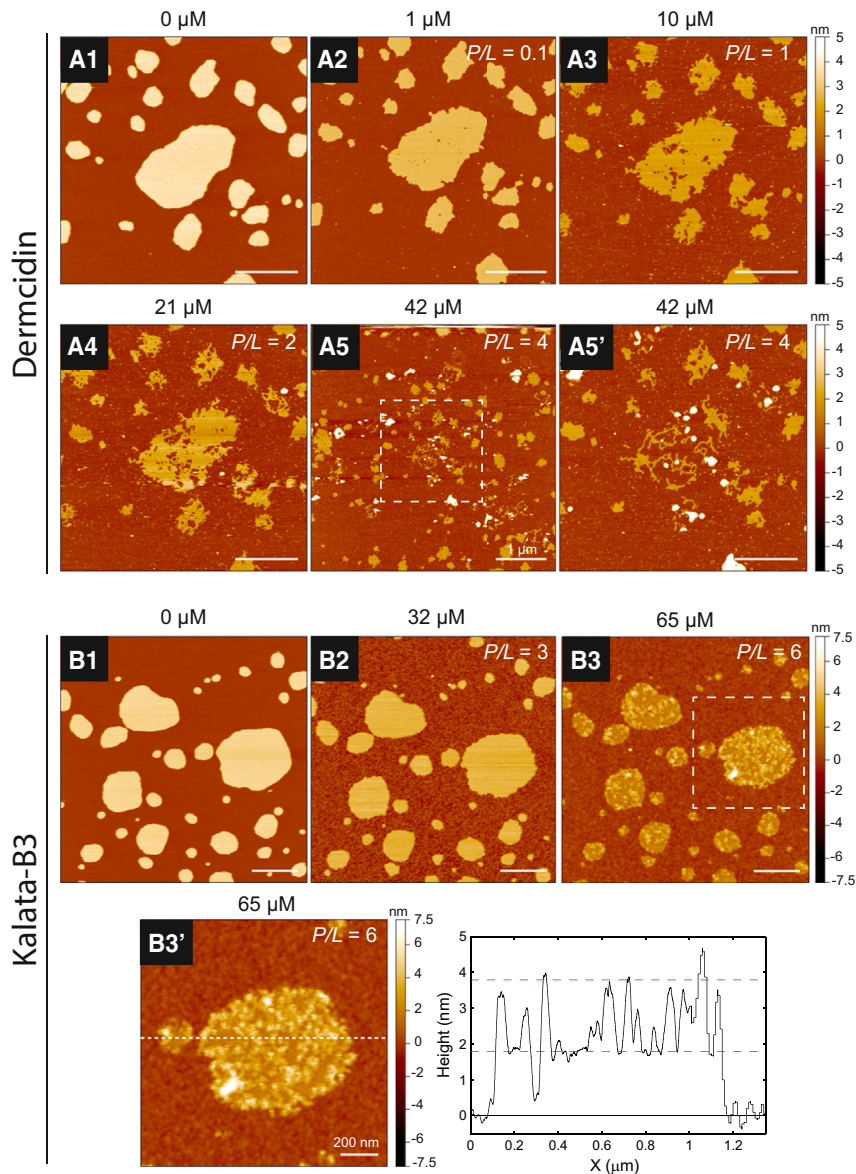


FIGURE 3 (A–F) Membrane structural transformations of DMPC bilayer patches induced by the positively charged AMPs aurein-1.1 (A), citropin-1.1 (B), magainin-1 (C), dermaseptin-1 (D), indolicidin (E), and HBD-1 (F). Bilayer patches were first imaged in the absence of peptide (A1, B1, C1, etc.) and then monitored through the course of successive peptide concentrations (increasing from left to right). (A) Increasing concentrations of aurein-1.1 revealed edge instability and a porated membrane (A2). Micrograph (A3) is from a separate experiment showcasing worm-like micelle formation by 3  $\mu$ M aurein-1.1. (B) Citropin-1.1 exhibited a similar response to aurein-1.1, displaying edge instability and a porated membrane (B2), with worm-like micelle formation (B3) occurring by 3  $\mu$ M. The concentration responses of magainin-1, dermaseptin-1, and indolicidin were similar, as the onset of micellization (C3, D3, and E3) occurred in the same range below 0.5  $\mu$ M. The bilayer patch monitored through images (E1) and (E2) was inadvertently smeared, and a nearby patch (E3) on the substrate was chosen to obtain a high-resolution image of worm-like micelles induced by indolicidin. To better reveal the self-assembled structures, the dashed box in (E3) indicates a zoomed-in region shown in the inset (data scaled to a 5 nm range). (F) Although bilayer edge instability was observed at 0.3  $\mu$ M HBD-1 (F2), a significantly higher amount of peptide was needed to observe detergent behavior (F3). All images were obtained at 30°C. White scale bars are 500 nm unless otherwise indicated. To see this figure in color, go online.





**FIGURE 4** (A and B) Membrane structural transformations of DMPC bilayer patches induced by the negatively charged AMPs DCD (A) and KB3 (B). Bilayer patches in the absence of peptide (A1 and B1) were monitored through the course of increasing peptide concentrations. (A) DCD exhibited a noticeable line-active behavior from an observed expanded bilayer edge (A2). The number and size of porous defects within the bilayer core grew (A3 and A4), and eventually the integrity of the membrane was fully compromised as micellization resulted (A5). (B) KB3 exhibited less activity than DCD. Bilayer edge instability was not observed until 32  $\mu\text{M}$  KB3 (B2). Detergent behavior was less evident and the membrane was decorated with peripherally bound peptide (B3). A line section in (B3') shows that the features are  $\sim 2$  nm high from the surrounding surface. The dashed boxes in (A5) and (B3) indicate zoomed-in regions that are shown in (A5') and (B3'). All images were obtained at 30°C. White scale bars are 500 nm unless otherwise indicated. To see this figure in color, go online.

when permeabilizing pathogens (52–55). Paulmann et al. (52) showed that DCD preferentially forms a helical structure with negatively charged phosphoglycerol over zwitterionic phosphocholine membranes. High ionic strength and the presence of divalent cations, specifically  $\text{Zn}^{2+}$ , were shown to enhance DCD's channel-like behavior in membranes, to support a pore-forming model. Recently, Song et al. (53) posited that DCD forms a hexameric, barrel-stave channel in POPE/POPG membranes.

Our experiments suggest that a barrel-stave pore-forming model does not account for DCD's behavior. Fig. 4 A shows the membrane interaction of DCD as the bulk concentration was increased. Upon injection of 1  $\mu\text{M}$  DCD (Fig. 4 A2), a distinctive line-active behavior and several defects were observed within the bilayer core at this low concentration. Insertion of DCD into the DMPC bilayer was evidenced

by a relative thinning of the membrane as the bulk concentration was increased (Fig. 4, A1–A5). The bilayer edge continued to expand and the number and size of porous defects within the lamellar core increased, providing more edges to which DCD could adsorb. Ultimately, the detergent behavior of DCD resulted in micellization of the membrane into the bulk superphase at a final concentration of 42  $\mu\text{M}$  (Fig. 4 A5), where remaining lipid/peptide material on the mica surface assembled into worm-like micelles (Fig. 4 A5'). Clearly, DCD's action required a line geometry for favorable binding to cause such degradation of membrane integrity. Using AFM, Paulmann et al. (52) observed defect formation in supported POPC membranes when 2  $\mu\text{M}$  DCD was present. However, their study was limited to a single concentration and no detergent behavior was observed, precluding a line-active explanation for DCD's

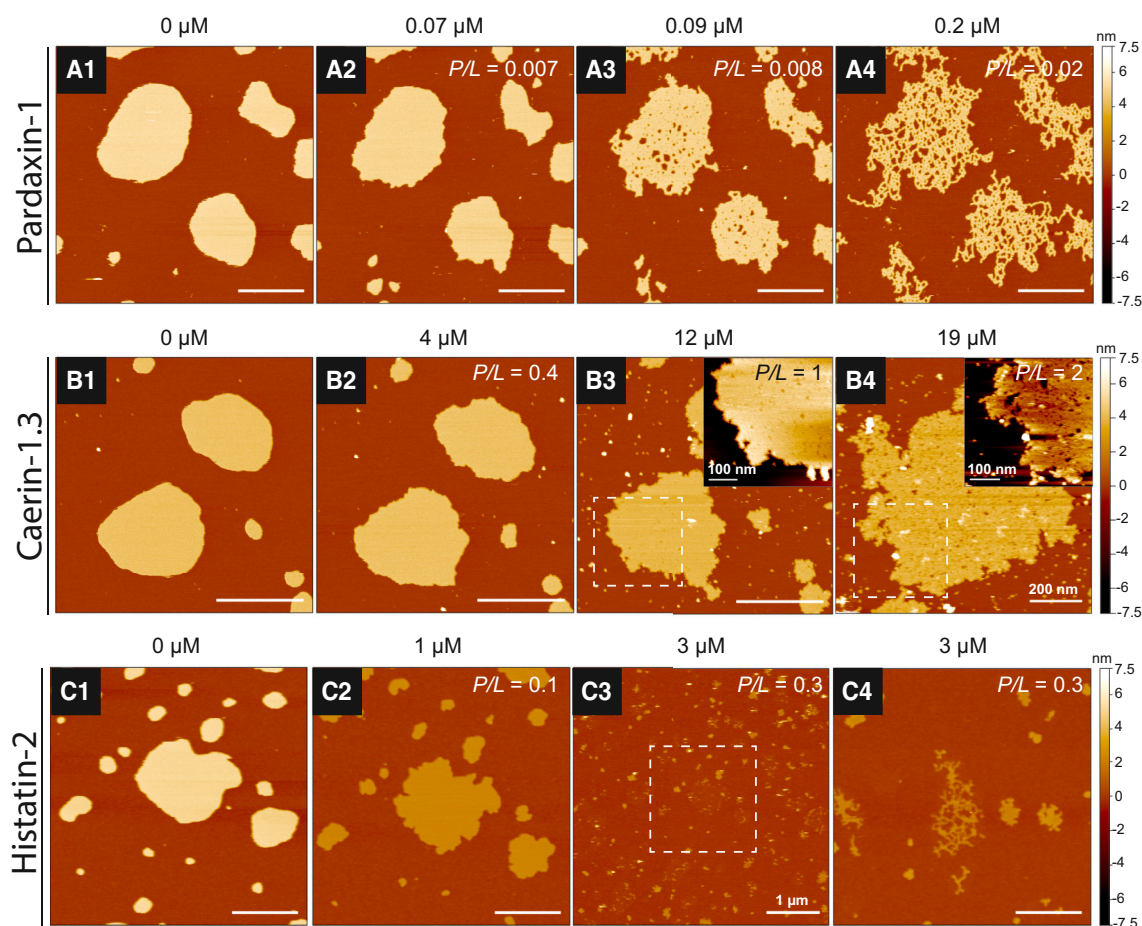


**FIGURE 5** (A–C) Membrane structural transformations of DMPC bilayer patches induced by the neutral AMPs pardaxin-1 (A), caerin-1.3 (B), and histatin-2 (C). Bilayer patches were first imaged in the absence of peptide (A1, B1, and C1) and then monitored through the course of successive peptide concentrations (increasing from left to right). (A) With increasing pardaxin-1, the bilayer underwent structural transformations exhibiting edge instability (A2), porous defects (A3), and finally worm-like micelles (A4) within a low concentration regime similar to that of PG-1, magainin-1, dermaseptin-1, and indolicidin. (B) The line activity of caerin-1.3 was evident from the bilayer edge instability observed at 4  $\mu\text{M}$  (B2) that caused porous defects to form within the core of the bilayer (B3) and led to micellization (B4). The bilayer patch monitored through images (B1)–(B3) was damaged from its softened state, and a nearby patch (B4) on the substrate was chosen to obtain a high-resolution image of the micellized state at 19  $\mu\text{M}$  caerin-1.3. To better reveal caerin-induced membrane transformations, the dashed boxes in (B3) and (B4) indicate zoomed-in regions shown in the inset (data scaled to a 5 nm range). (C) Edge instability and membrane thinning were observed upon introduction of 1  $\mu\text{M}$  histatin-2 (C2). (C3) Zoomed-out image showing bilayer solubilization in the surrounding area. A dashed box is included to indicate the scanning area corresponding to images (C1) and (C2). The sample was translated laterally to a new area (C4) to capture the presence of worm-like micelle structures. All images were obtained at 30°C. White scale bars are 500 nm unless otherwise indicated. To see this figure in color, go online.

behavior. It is possible that the contiguous membrane used in their study prevented peptide insertion, since room for bilayer expansion was constrained. As ALM did not show line activity, we concluded that a barrel-stave pore is unlikely for DCD, given the observed membrane disruption in our study.

In contrast, the onset of KB3 activity with DMPC membranes (Fig. 4 B) was shifted to a higher dosage regime as compared with DCD, as no significant bilayer changes were observed below 32  $\mu\text{M}$ . The membrane interaction of kalata cyclotides has a lipid headgroup preference, and a higher binding affinity has been observed with phosphoethanolamine compared with phosphocholine lipids (55,56). This helps to explain why higher amounts of KB3 were

needed for us to see detergent-like behavior in our experimental system. Upon incubation with 32  $\mu\text{M}$  KB3 (Fig. 4 B2), membrane thinning and disruption at the bilayer edge were observed. Additionally, the surrounding bare mica surface was covered by the apparent, nonspecific adsorption of the peptides. The line activity we observed for KB3 does not agree with the AFM results of Hall et al. (56), who reported that no bilayer structural transformations were seen in DMPC membranes upon addition of 10  $\mu\text{M}$  kalata-B1. At a concentration of 65  $\mu\text{M}$  KB3 (Fig. 4 B3), the surface of the bilayer became decorated with aggregates, presumably made of peptide, that were  $\sim 2$  nm high from the undecorated portion of the bilayer. Kalata peptides can self-associate to form tetramers in solution,



suggesting that an oligomerized state may be important for their membrane binding and possible pore formation (57). Using coarse-grained MD simulations, Nawae et al. (58) showed that kalata-B1 remained peripherally bound and did not penetrate deeply into the membrane to form well-organized pores. Instead, the cyclotides clustered on the surface, resulting in curvature deformation of the membrane. The low penetration depth is likely a consequence of the facial organization of the hydrophobes (Fig. S3 B) that creates a shallow surface for membrane insertion, a trait of kalata cyclotides (50). Moreover, Nawae et al. (58) reported that the center of mass of kalata-B1 on the membrane was on average 1.9 nm from the center of mass of the lipid headgroups. Our line section analysis resulted in a nearly identical value and supports the conclusion that the aggregates on the membrane (Fig. 4 B3) are interfacially bound KB3 peptides. Subsequent time-lapse imaging (Fig. S9) revealed slow membrane solubilization into the superphase.

We have shown that both positively and negatively charged AMPs share a line-active behavior in their mechanism for inducing membrane disruption. Curiously, lower-charge peptides and higher-charge peptides were observed to disrupt membranes at similar concentrations. This was especially clear when the interactions of magainin-1 (+3), dermaseptin-1 (+3), and indolicidin (+4) were juxtaposed with those of PG-1 (+7), as all reached a final micellized state at a maximum concentration of 1  $\mu$ M. Although HBD-1 has a +4 charge, much higher peptide concentrations were required to completely disrupt the membrane, and its response even differed by two orders of magnitude when compared with indolicidin (+4).

The apparent lack of a charge-dependent effect on the concentration response of the peptides was further reinforced when we examined the interaction of neutral AMPs (Fig. 5). Pardaxin-1 and caerin-1.3 share similar secondary structures characterized by helix-hinge-helix motifs (59,60) and are thought to form barrel-stave pores (pardaxin) and toroidal pores (caerin) (11,15). The exact structure of histatin-2 when membrane bound remains unknown; however, work on the related histatin-5 indicates that C-terminal  $\alpha$ -helical content is important for its bactericidal activity (61). A putative zinc-binding motif has been implicated in the stabilization of secondary structure in histatins in the presence of negatively charged membranes (62). Mechanistically, the membrane interaction of histatins remains largely unknown, and our AFM results represent a unique investigation of these poorly studied AMPs. Fig. 5, A2, B2, and C2, show that pardaxin-1, caerin-1.3, and histatin-2 display characteristic line-active behavior, as evidenced by the morphological changes that occurred at the bilayer edge. Increasing concentrations led to the formation of porous defects (Fig. 5, A3 and B3) and eventually to complete disruption of the bilayer patches. Zemel et al. (63) showed computationally that neutral to weakly charged peptides form barrel-stave pores and that higher peptide

charges are needed to favor toroidal-pore formation, suggesting that line activity is only present with charged peptides. Our investigations reveal that, with the exception of ALM, all of the AMPs we studied exhibited line activity despite having different charges and concentration responses.

### Molecular origins that drive line-active behavior

Given the ability of AMPs to lower line tension independently of charge, it is energetically favorable for the peptides to bind at the edge, increasing the P/L ratio in the membrane that drives structural transformations. A potential molecular origin of line activity is the adoption of amphipathic secondary structures. Segregation of hydrophobic and hydrophilic amino acid residues in spatially arranged faces affords AMPs the ability to favorably partition and insert into membranes. For instance, the disulfide bonds present in  $\beta$ -sheet peptides, such as PG-1 and human defensins, create stable amphiphilic structures, as a reduction of these covalent linkages was shown to diminish their membrane lytic activity (64,65). The interfacial activity model proposed by Wimley (66) emphasizes the altered packing and organization of lipids that results from imperfect amphipathic secondary structures. These imperfect structures can be consequences of poor segregation of hydrophilic/hydrophobic residues or deviations of the peptide from ideal secondary structures. They distort the membrane in a way that accommodates the apolar, polar, and charged groups of the peptide distributed along the structure. The emphasis on altered packing and organization of lipids upon peptide partitioning accords with the work of Huang and co-workers (36–38), which showed that surface-bound AMPs elastically thin membranes, and with studies by Bechinger (67) and Zemel et al. (68) that correlated peptide shape with the induction of membrane curvature strain. In essence, AMPs can be assumed to have intrinsic curvatures (e.g., a wedge), and their incorporation into the membrane can transform it into different structures limited by the molecular dimensions of the peptide. This is related in part to the behavior of proteins in the Bin/Amphiphysin/Rvs-domain superfamily, variants of which display positive or negative spontaneous curvatures that are needed to stabilize common cell membrane topologies found in endo- and exocytotic events and in membrane protrusions (69).

Using MD simulations, Lazaridis and coworkers (35,45,70) convincingly showed the effects that imperfect amphipathic structures have on the generation of barrel-stave or toroidal pores. For instance, when they investigated K7Q or K7A in silico mutants of melittin, they found that preformed barrel-stave pores did not evolve into toroidal pores. In contrast, when Gln7 was mutated to Lys in ALM, barrel-stave pores were not stable and toroidal pores were formed. These results indicated that a nonuniform

charge distribution along the peptide structure is a critical factor in organizing phospholipids into the curved configuration found in toroidal pores (70). Moreover, when melittin's structure was made to be a more ideal, linear helix through Leu mutation of two charged residues found along its hydrophobic face, the initial cylindrical pore remained stable. This finding suggested that the more-ideal amphiphilic structure deterred the induction of membrane curvature. Combined, these results implicate the overall peptide structure and the distribution of charged residues in line-active behavior.

Many of the peptides we investigated displayed an imperfect amphiphilic structure (Figs. S1–S4) resulting from poor segregation of apolar and polar residues, or exhibited deviations from ideal secondary structural motifs, such as the breaking of an ideal helix into more flexible helix-hinge-helix constructs. A comparison of indolicidin and PG-1 demonstrates the effect that an imperfect amphiphilic secondary structure has on line activity. Although they differ in charge and structure, they both transform the membrane into worm-like micelles within almost identical concentration regimes. Whereas indolicidin assumes a random, linear conformation, PG-1 has a well-defined  $\beta$ -hairpin; however, both share a similar planar amphiphilicity with a central hydrophobic zone bounded by clusters of Arg residues (Figs. S1 B and S2 E). Tang et al. (71) showed that for an inserted state, the Arg residues of PG-1 make proximal guanidinium-phosphate connections that may underlie the lipid orientational changes necessary for the formation of toroidal pores. Hence, the line-active behavior we observe for both indolicidin and PG-1 may depend on the terminal placement of these residues so that they can interact simultaneously with both membrane leaflets.

The line activity of the  $\alpha$ -helical peptides studied here seems to be governed by their ability to achieve imperfect helical arrangements that optimize polar and apolar interactions across the membrane. A flexible hinge region bounded by Pro15 and Pro19 in caerin-1.3 (60) and the subtle bend in magainin-1 from a Gly(X<sub>4</sub>)Gly motif, which is known to arc related piscidin peptides (72), cause both caerin-1.3 and magainin-1 to adopt curved architectures necessary for their biological activity. For example, Fernandez et al. (73) showed that in the caerin-related peptide maculatin-1.1, mutation of the arc-inducing Pro15 residue lowered its membrane-disrupting capabilities. The Gly(X<sub>4</sub>)Gly motif is also seen between Gly18 and Gly23 in the primary sequence of dermaseptin-1, where four Lys residues span the length of the structure. Additionally, Mihajlovic and Lazaridis (70) noted that Lys4 in an analog of magainin is a more important residue for toroidal-pore formation than the other lysines positioned in the middle of the helix (Lys11 and Lys14), and implicates the N-terminal Lys in the line activity of both magainin-1 and dermaseptin-1. We observed that magainin-1 and dermaseptin-1 caused membrane micellization at nearly the same concentration, whereas aurein-1.1 and

citropin-1.1 interacted at slightly higher concentrations. This suggests that peptides that can easily insert into and span the length of a membrane are more effective at forming line geometries, as key residues are positioned to facilitate distortion of the membrane into a curved edge. The helix-bend-helix motifs present in pardaxin and DCD ensure that a C-terminal portion of the peptide can span a membrane and an N-terminal helix can lie along the membrane surface (52,59). As can be seen in the secondary-structure representation for both DCD and pardaxin-1 (Figs. S3 A and S4 A), this break in the ideal helical structure primes the N-terminal Lys residue at the headgroup interface through surface-lying helices. Although the exact structure of histatin-2 remains to be determined in a membrane-mimetic environment, it is suggestive that both Lys and Arg residues (Arg1, Lys2, Lys6, and Arg11) are clustered within the N-terminal half of the peptide.

The guanidinium group of Arg has been proposed to be a greater inducer of membrane curvature than the primary amine group of Lys, given its bidentate hydrogen binding (14).  $\beta$ -sheet-containing peptides have a higher Arg content as compared with  $\alpha$ -helical peptides, and when we examined the interaction of HBD-1 and KB3, we found that both were less line-active than PG-1 and indolicidin, as higher concentrations were needed to elicit an interaction with DMPC bilayers. The lower activity of HBD-1 and KB3 may result from a more diffuse distribution of charged residues and the presence of a flat, hydrophobic face, which, as noted in the case of KB3, presumably keeps the peptides peripherally bound. Schmidt et al. (14) suggested a condition in which peptides with lower Arg contents can still induce curved membrane topologies by offsetting to higher contents of Lys and hydrophobic residues. Fig. S10, A and B, show the primary sequence analysis of our line-active peptides, which we performed in a manner similar to that described by Schmidt et al. (14) and Mishra et al. (74). Although our sample size is small, we are in agreement that the  $\alpha$ -helical AMPs examined tend to have higher average hydrophobicities and greater Lys contents as compared with their  $\beta$ -sheet counterparts (Fig. S10 A). Moreover, peptides that are line-active at lower concentrations have higher fractions of total Lys and Arg residues in their primary sequence (see Fig. S10 B). However, there are exceptions to the rule: caerin-1.3 has no positive residues within its primary sequence but can still impart its line activity within a moderate concentration regime, and HBD-1 has a fairly high fraction of total positive charges and requires higher concentrations as compared with other positively charged AMPs to cause complete membrane disruption. Theoretically, peptides with nearly identical Kyte-Doolittle hydrophathy values would partition similarly to zwitterionic DMPC bilayers; however, the line activities of PG-1 (−0.25), KB3 (−0.20), and HBD-1 (−0.27) display drastically different concentration responses. Our examination suggests that a simple categorization of AMPs based on

their overall Arg and Lys contents may not be a direct indicator of their eventual membrane line activity. Instead, our data show that membrane distortion results from a more complex interplay between peptide structure and the distribution of these key residues.

## CONCLUSIONS

Collectively, our results show that AMPs share a common ability to reduce membrane line tension in a concentration-dependent manner that is physically similar to the action of simple detergents. Reduction of the line tension from the edge adsorption of these peptides (referred to as linactants due to their line activities) causes the edge contour to expand, and in turn enables further binding events at the edge that increase the P/L ratio in the membrane. With further increases in the bulk peptide concentration, the accumulated surface density is able to reach a critical stage for peptide insertion into the bilayer. The critical concentration necessary for AMP insertion would therefore be dependent on factors that modulate peptide partitioning to the membrane, such as lipid headgroup specificity (75,76), packing defects (77,78), and line interfaces at phase boundaries (79–81). The creation of new edges within the bilayer facilitates the binding of more AMPs, further reducing the bilayer line tension. Ultimately, the lamellar organization of the membrane is transformed into new peptide-lipid self-assembled structures that are limited in scale by the molecular dimensions of the peptide itself. Although an exposed edge does not initially exist in a cell membrane, this positively reinforcing condition will become evident once an initial edge geometry is created within the membrane from peptide insertion. The self-assembled structures that we observed through the course of AMP-induced membrane disruption, culminating in the formation of worm-like micelles, could not be explained by a pore-only model. Rather, a common reduction of line tension may underlie AMP activity and appears to be biologically relevant, as membrane protrusions resembling worm-like micelles have been observed to emanate from AMP-exposed bacteria (82–84).

Careful selection of a variety of peptides that differ in both charge and secondary structure revealed important physical parameters that affect the observed line-active behavior. With the exception of the most hydrophobic peptide, ALM, which exhibited no line activity, more polar peptides that exhibited line activity were surprisingly invariant in their concentration response with respect to their overall charge. The ability of positive, negative, and neutral AMPs to utilize a common line-active mechanism in their interaction with membranes challenges the prevailing electrostatic model of AMP selectivity and its general application to all membrane-active AMPs. Instead, factors such as membrane fluidity and lipid acyl chain length are relevant parameters that modulate the ability of AMPs to distort the membrane

into the geometries necessary for their favorable incorporation into the membrane.

The line-active behavior of the AMPs correlated with their adoption of imperfect secondary structures resulting from either poor amphiphilic segregation of residues or breaks in the symmetry of ideal secondary motifs, such as flexible kinks introduced into linear helices. As a consequence of these structural imperfections, polar residues (typically Lys and Arg) were strategically placed at the periphery of the membrane for subsequent reorganization of the phospholipids. Moreover, the type of secondary motif employed by an AMP did not ultimately determine its line activity, as peptides with  $\alpha$ -helical,  $\beta$ -sheet, and even random, linear backbone configurations (e.g., indolicidin) exhibited similar detergent-like behavior. We speculate that this interplay of peptide structure and the manner in which polar residues are distributed in relation to the membrane governs the line activity of AMPs. Future experiments to investigate the positional placement of Lys and Arg residues along a given AMP would clarify the role that residue distribution has in modulating line activity. Additionally, by systematically altering the degree of rotational amphiphilicity present in antimicrobial polypeptides, as recently developed by Xiong et al. (85), the role of imperfect amphiphilicity in peptide structures can be more definitively correlated with AMP line activity. Future work should also examine the role of negatively charged residues in line-active behavior, given that caerin-1.3, lacking both Lys and Arg residues, exhibited line activity within a moderate concentration regime.

## SUPPORTING MATERIAL

Supporting Materials and Methods, ten figures, and two tables are available at [http://www.biophysj.org/biophysj/supplemental/S0006-3495\(16\)30888-8](http://www.biophysj.org/biophysj/supplemental/S0006-3495(16)30888-8).

## AUTHOR CONTRIBUTIONS

J.M.H. and K.Y.C.L. conceived the study and designed the experiments. J.M.H. performed the research and wrote the manuscript with contributions from A.J.W., F.S., and K.Y.C.L. All authors discussed the results and commented on the manuscript.

## ACKNOWLEDGMENTS

We thank Drs. Justin Jureller and Qiti Guo (The University of Chicago Materials Research Science and Engineering Center) for their training and help in using the Asylum Cypher ES atomic force microscope, and their general expertise in scanning probe microscopy throughout the course of this research. We also thank Dr. Elena Solomaha (Biophysics Core, The University of Chicago) for her assistance in data collection in the calcein leakage experiments.

This research was supported by the National Science Foundation (NSF; MCB-1413613) and the NSF-supported MRSEC program at the University of Chicago (DMR-1420709). The Asylum Cypher ES atomic force

microscope was made possible by an NSF Materials Research Instrumentation Grant (DMR-1429550).

## REFERENCES

- Hughes, J. M. 2011. Preserving the lifesaving power of antimicrobial agents. *JAMA*. 305:1027–1028.
- Zaslouf, M. 2002. Antimicrobial peptides of multicellular organisms. *Nature*. 415:389–395.
- Henderson, J. M., and K. Y. C. Lee. 2013. Promising antimicrobial agents designed from natural peptide templates. *Curr. Opin. Solid State Mater. Sci.* 17:175–192.
- Baumann, G., and P. Mueller. 1974. A molecular model of membrane excitability. *J. Supramol. Struct.* 2:538–557.
- Christensen, B., J. Fink, ..., D. Mauzerall. 1988. Channel-forming properties of cecropins and related model compounds incorporated into planar lipid membranes. *Proc. Natl. Acad. Sci. USA*. 85:5072–5076.
- Rapaport, D., and Y. Shai. 1991. Interaction of fluorescently labeled pardaxin and its analogues with lipid bilayers. *J. Biol. Chem.* 266:23769–23775.
- Matsuzaki, K., O. Murase, ..., K. Miyajima. 1996. An antimicrobial peptide, magainin 2, induced rapid flip-flop of phospholipids coupled with pore formation and peptide translocation. *Biochemistry*. 35: 11361–11368.
- Yang, L., T. A. Harroun, ..., H. W. Huang. 2001. Barrel-stave model or toroidal model? A case study on melittin pores. *Biophys. J.* 81:1475–1485.
- Qian, S., W. Wang, ..., H. W. Huang. 2008. Structure of transmembrane pore induced by Bax-derived peptide: evidence for lipidic pores. *Proc. Natl. Acad. Sci. USA*. 105:17379–17383.
- Pieta, P., J. Mirza, and J. Lipkowski. 2012. Direct visualization of the alamethicin pore formed in a planar phospholipid matrix. *Proc. Natl. Acad. Sci. USA*. 109:21223–21227.
- Hallock, K. J., D.-K. Lee, ..., A. Ramamoorthy. 2002. Membrane composition determines pardaxin's mechanism of lipid bilayer disruption. *Biophys. J.* 83:1004–1013.
- Yang, L., T. M. Weiss, ..., H. W. Huang. 2000. Crystallization of antimicrobial pores in membranes: magainin and protegrin. *Biophys. J.* 79:2002–2009.
- Yamaguchi, S., T. Hong, ..., M. Hong. 2002. Solid-state NMR investigations of peptide-lipid interaction and orientation of a  $\beta$ -sheet antimicrobial peptide, protegrin. *Biochemistry*. 41:9852–9862.
- Schmidt, N. W., A. Mishra, ..., G. C. L. Wong. 2011. Criterion for amino acid composition of defensins and antimicrobial peptides based on geometry of membrane destabilization. *J. Am. Chem. Soc.* 133:6720–6727.
- Chen, R., and A. E. Mark. 2011. The effect of membrane curvature on the conformation of antimicrobial peptides: implications for binding and the mechanism of action. *Eur. Biophys. J.* 40:545–553.
- Shai, Y. 1999. Mechanism of the binding, insertion and destabilization of phospholipid bilayer membranes by  $\alpha$ -helical antimicrobial and cell non-selective membrane-lytic peptides. *Biochim. Biophys. Acta*. 1462:55–70.
- Fernandez, D. I., A. P. Le Brun, ..., F. Separovic. 2012. The antimicrobial peptide aurein 1.2 disrupts model membranes via the carpet mechanism. *Phys. Chem. Chem. Phys.* 14:15739–15751.
- Ambroggio, E. E., F. Separovic, ..., L. A. Bagatolli. 2005. Direct visualization of membrane leakage induced by the antibiotic peptides: maculatin, citropin, and aurein. *Biophys. J.* 89:1874–1881.
- Wang, Z., and G. Wang. 2004. APD: the Antimicrobial Peptide Database. *Nucleic Acids Res.* 32:D590–D592.
- Wimley, W. C., and K. Hristova. 2011. Antimicrobial peptides: successes, challenges and unanswered questions. *J. Membr. Biol.* 239: 27–34.
- Nguyen, L. T., E. F. Haney, and H. J. Vogel. 2011. The expanding scope of antimicrobial peptide structures and their modes of action. *Trends Biotechnol.* 29:464–472.
- Yount, N. Y., and M. R. Yeaman. 2004. Multidimensional signatures in antimicrobial peptides. *Proc. Natl. Acad. Sci. USA*. 101:7363–7368.
- Lam, K. L. H., Y. Ishitsuka, ..., K. Y. C. Lee. 2006. Mechanism of supported membrane disruption by antimicrobial peptide protegrin-1. *J. Phys. Chem. B*. 110:21282–21286.
- Lam, K. L. H., H. Wang, ..., K. Y. C. Lee. 2012. Mechanism of structural transformations induced by antimicrobial peptides in lipid membranes. *Biochim. Biophys. Acta*. 1818:194–204.
- Zhang, L., R. Vidu, ..., P. Stroeve. 2002. Electrochemical and surface properties of solid-supported, mobile phospholipid bilayers on a polyanion/alkylthiol layer pair used for detection of antimicrobial peptide insertion. *Langmuir*. 18:1318–1331.
- Johnson, S. J., T. M. Bayerl, ..., E. Sackmann. 1991. Structure of an adsorbed dimyristoylphosphatidylcholine bilayer measured with specular reflection of neutrons. *Biophys. J.* 59:289–294.
- Kučerka, N., M. A. Kiselev, and P. Balgavý. 2004. Determination of bilayer thickness and lipid surface area in unilamellar dimyristoylphosphatidylcholine vesicles from small-angle neutron scattering curves: a comparison of evaluation methods. *Eur. Biophys. J.* 33:328–334.
- Smith, A. M., M. Vinchurkar, ..., A. N. Parikh. 2010. Order at the edge of the bilayer: membrane remodeling at the edge of a planar supported bilayer is accompanied by a localized phase change. *J. Am. Chem. Soc.* 132:9320–9327.
- Lee, K. Y. C., and H. M. McConnell. 1993. Quantized symmetry of liquid monolayer domains. *J. Phys. Chem.* 97:9532–9539.
- Fošnarič, M., V. Kralj-Iglič, ..., S. May. 2003. Stabilization of pores in lipid bilayers by anisotropic inclusions. *J. Phys. Chem. B*. 107:12519–12526.
- Karatekin, E., O. Sandre, ..., F. Brochard-Wyart. 2003. Cascades of transient pores in giant vesicles: line tension and transport. *Biophys. J.* 84:1734–1749.
- Puech, P.-H., N. Borghi, ..., F. Brochard-Wyart. 2003. Line thermodynamics: adsorption at a membrane edge. *Phys. Rev. Lett.* 90:128304.
- de Joannis, J., F. Y. Jiang, and J. T. Kindt. 2006. Coarse-grained model simulations of mixed-lipid systems: composition and line tension of a stabilized bilayer edge. *Langmuir*. 22:998–1005.
- Moldovan, D., D. Pinisetty, and R. V. Devireddy. 2007. Molecular dynamics simulation of pore growth in lipid bilayer membranes in the presence of edge-active agents. *Appl. Phys. Lett.* 91:204104.
- Lazaridis, T., Y. He, and L. Prieto. 2013. Membrane interactions and pore formation by the antimicrobial peptide protegrin. *Biophys. J.* 104:633–642.
- Chen, F.-Y., M.-T. Lee, and H. W. Huang. 2003. Evidence for membrane thinning effect as the mechanism for peptide-induced pore formation. *Biophys. J.* 84:3751–3758.
- Ludtke, S., K. He, and H. Huang. 1995. Membrane thinning caused by magainin 2. *Biochemistry*. 34:16764–16769.
- Heller, W. T., A. J. Waring, ..., H. W. Huang. 2000. Membrane thinning effect of the  $\beta$ -sheet antimicrobial protegrin. *Biochemistry*. 39: 139–145.
- Jiang, Y., H. Wang, and J. T. Kindt. 2010. Atomistic simulations of bicelle mixtures. *Biophys. J.* 98:2895–2903.
- Haustein, M., M. Wahab, ..., P. Schiller. 2015. Vesicle solubilization by bile salts: comparison of macroscopic theory and simulation. *Langmuir*. 31:4078–4086.
- Huang, H. W. 1995. Elasticity of lipid bilayer interacting with amphiphilic helical peptides. *J. Phys. B At. Mol. Opt. Phys.* 5:1427–1431.
- Liu, D., and W. F. DeGrado. 2001. De novo design, synthesis, and characterization of antimicrobial  $\beta$ -peptides. *J. Am. Chem. Soc.* 123:7553–7559.



43. Gregory, S. M., A. Pokorny, and P. F. Almeida. 2009. Magainin 2 revisited: a test of the quantitative model for the all-or-none permeabilization of phospholipid vesicles. *Biophys. J.* 96:116–131.
44. Hovakemian, S. G., R. Liu, ..., H. Heerklottz. 2015. Correlating antimicrobial activity and model membrane leakage induced by nylon-3 polymers and detergents. *Soft Matter*. 11:6840–6851.
45. Mihajlovic, M., and T. Lazaridis. 2010. Antimicrobial peptides bind more strongly to membrane pores. *Biochim. Biophys. Acta.* 1798:1494–1502.
46. Sun, D., J. Forsman, and C. E. Woodward. 2015. Amphipathic membrane-active peptides recognize and stabilize ruptured membrane pores: exploring cause and effect with coarse-grained simulations. *Langmuir* 31:752–761.
47. Rakowska, P. D., H. Jiang, ..., M. G. Ryadnov. 2013. Nanoscale imaging reveals laterally expanding antimicrobial pores in lipid bilayers. *Proc. Natl. Acad. Sci. USA.* 110:8918–8923.
48. Schitteck, B., R. Hipfel, ..., C. Garbe. 2001. Dermcidin: a novel human antibiotic peptide secreted by sweat glands. *Nat. Immunol.* 2:1133–1137.
49. Jung, H. H., S.-T. Yang, ..., J. I. Kim. 2010. Analysis of the solution structure of the human antibiotic peptide dermcidin and its interaction with phospholipid vesicles. *BMB Rep.* 43:362–368.
50. Shenkarev, Z. O., K. D. Nadezhdin, ..., A. S. Arseniev. 2006. Conformation and mode of membrane interaction in cyclotides. Spatial structure of kalata B1 bound to a dodecylphosphocholine micelle. *FEBS J.* 273:2658–2672.
51. Tam, J. P., Y.-A. Lu, ..., K.-W. Chiu. 1999. An unusual structural motif of antimicrobial peptides containing end-to-end macrocycle and cysteine-knot disulfides. *Proc. Natl. Acad. Sci. USA.* 96:8913–8918.
52. Paulmann, M., T. Arnold, ..., B. Schitteck. 2012. Structure-activity analysis of the dermcidin-derived peptide DCD-1L, an anionic antimicrobial peptide present in human sweat. *J. Biol. Chem.* 287:8434–8443.
53. Song, C., C. Weichbrodt, ..., K. Zeth. 2013. Crystal structure and functional mechanism of a human antimicrobial membrane channel. *Proc. Natl. Acad. Sci. USA.* 110:4586–4591.
54. Huang, Y.-H., M. L. Colgrave, ..., D. J. Craik. 2009. The biological activity of the prototypic cyclotide kalata b1 is modulated by the formation of multimeric pores. *J. Biol. Chem.* 284:20699–20707.
55. Wang, C. K., H. P. Wacklin, and D. J. Craik. 2012. Cyclotides insert into lipid bilayers to form membrane pores and destabilize the membrane through hydrophobic and phosphoethanolamine-specific interactions. *J. Biol. Chem.* 287:43884–43898.
56. Hall, K., T.-H. Lee, ..., M.-I. Aguilar. 2012. Gly6 of kalata B1 is critical for the selective binding to phosphatidylethanolamine membranes. *Biochim. Biophys. Acta.* 1818:2354–2361.
57. Nourse, A., M. Trabi, ..., D. J. Craik. 2004. A comparison of the self-association behavior of the plant cyclotides kalata B1 and kalata B2 via analytical ultracentrifugation. *J. Biol. Chem.* 279:562–570.
58. Nawae, W., S. Hannongbua, and M. Ruengjitchachawalya. 2014. Defining the membrane disruption mechanism of kalata B1 via coarse-grained molecular dynamics simulations. *Sci. Rep.* 4:3933.
59. Bhunia, A., P. N. Domadia, ..., S. Bhattacharjya. 2010. NMR structure of pardaxin, a pore-forming antimicrobial peptide, in lipopolysaccharide micelles: mechanism of outer membrane permeabilization. *J. Biol. Chem.* 285:3883–3895.
60. Pukala, T. L., C. S. Brinkworth, ..., J. H. Bowie. 2004. Investigating the importance of the flexible hinge in caerin 1.1: solution structures and activity of two synthetically modified caerin peptides. *Biochemistry.* 43:937–944.
61. Raj, P. A., M. Edgerton, and M. J. Levine. 1990. Salivary histatin 5: dependence of sequence, chain length, and helical conformation for candidacidal activity. *J. Biol. Chem.* 265:3898–3905.
62. Melino, S., S. Rufini, ..., R. Petruzzelli. 1999. Zn<sup>2+</sup> ions selectively induce antimicrobial salivary peptide histatin-5 to fuse negatively charged vesicles. Identification and characterization of a zinc-binding motif present in the functional domain. *Biochemistry.* 38:9626–9633.
63. Zemel, A., D. R. Fattal, and A. Ben-Shaul. 2003. Energetics and self-assembly of amphipathic peptide pores in lipid membranes. *Biophys. J.* 84:2242–2255.
64. Harwig, S. S. L., A. Waring, ..., R. I. Lehrer. 1996. Intramolecular disulfide bonds enhance the antimicrobial and lytic activities of protegrins at physiological sodium chloride concentrations. *Eur. J. Biochem.* 240:352–357.
65. Wanniarachchi, Y. A., P. Kaczmarek, ..., E. M. Nolan. 2011. Human defensin 5 disulfide array mutants: disulfide bond deletion attenuates antibacterial activity against *Staphylococcus aureus*. *Biochemistry.* 50:8005–8017.
66. Wimley, W. C. 2010. Describing the mechanism of antimicrobial peptide action with the interfacial activity model. *ACS Chem. Biol.* 5:905–917.
67. Bechinger, B. 2009. Rationalizing the membrane interactions of cationic amphipathic antimicrobial peptides by their molecular shape. *Curr. Opin. Colloid Interface Sci.* 14:349–355.
68. Zemel, A., A. Ben-Shaul, and S. May. 2008. Modulation of the spontaneous curvature and bending rigidity of lipid membranes by interfacially adsorbed amphipathic peptides. *J. Phys. Chem. B.* 112:6988–6996.
69. Simunovic, M., G. A. Voth, ..., P. Bassereau. 2015. When physics takes over: BAR proteins and membrane curvature. *Trends Cell Biol.* 25:780–792.
70. Mihajlovic, M., and T. Lazaridis. 2012. Charge distribution and imperfect amphipathicity affect pore formation by antimicrobial peptides. *Biochim. Biophys. Acta.* 1818:1274–1283.
71. Tang, M., A. J. Waring, and M. Hong. 2007. Phosphate-mediated arginine insertion into lipid membranes and pore formation by a cationic membrane peptide from solid-state NMR. *J. Am. Chem. Soc.* 129:11438–11446.
72. Perrin, B. S., Jr., Y. Tian, ..., M. L. Cotten. 2014. High-resolution structures and orientations of antimicrobial peptides piscidin 1 and piscidin 3 in fluid bilayers reveal tilting, kinking, and bilayer immersion. *J. Am. Chem. Soc.* 136:3491–3504.
73. Fernandez, D. I., T.-H. Lee, ..., F. Separovic. 2013. Proline facilitates membrane insertion of the antimicrobial peptide maculatin 1.1 via surface indentation and subsequent lipid disordering. *Biophys. J.* 104:1495–1507.
74. Mishra, A., G. H. Lai, ..., G. C. L. Wong. 2011. Translocation of HIV TAT peptide and analogues induced by multiplexed membrane and cytoskeletal interactions. *Proc. Natl. Acad. Sci. USA.* 108:16883–16888.
75. Ishitsuka, Y., D. S. Pham, ..., K. Y. C. Lee. 2006. Insertion selectivity of antimicrobial peptide protegrin-1 into lipid monolayers: effect of head group electrostatics and tail group packing. *Biochim. Biophys. Acta.* 1758:1450–1460.
76. Arouri, A., A. Kerth, ..., A. Blume. 2011. The binding of an amphipathic peptide to lipid monolayers at the air/water interface is modulated by the lipid headgroup structure. *Langmuir* 27:2811–2818.
77. Strandberg, E., D. Tiltak, ..., A. S. Ulrich. 2012. Lipid shape is a key factor for membrane interactions of amphipathic helical peptides. *Biochim. Biophys. Acta.* 1818:1764–1776.
78. Garten, M., C. Prévost, ..., S. Vanni. 2015. Methyl-branched lipids promote the membrane adsorption of  $\alpha$ -synuclein by enhancing shallow lipid-packing defects. *Phys. Chem. Chem. Phys.* 17:15589–15597.
79. Shaw, J. E., R. F. Epanand, ..., C. M. Yip. 2008. Cationic peptide-induced remodeling of model membranes: direct visualization by in situ atomic force microscopy. *J. Struct. Biol.* 162:121–138.
80. Nicolini, C., J. Baranski, ..., R. Winter. 2006. Visualizing association of N-ras in lipid microdomains: influence of domain structure and interfacial adsorption. *J. Am. Chem. Soc.* 128:192–201.
81. Hutchison, J. B., R. M. Weis, and A. D. Dinsmore. 2012. Change of line tension in phase-separated vesicles upon protein binding. *Langmuir* 28:5176–5181.

82. Gidalevitz, D., Y. Ishitsuka, ..., K. Y. C. Lee. 2003. Interaction of antimicrobial peptide protegrin with biomembranes. *Proc. Natl. Acad. Sci. USA*. 100:6302–6307.
83. Lehrer, R. I., J. Andrew Tincu, ..., A. J. Waring. 2003. Natural peptide antibiotics from tunicates: structures, functions and potential uses. *Integr. Comp. Biol.* 43:313–322.
84. Rabanal, F., A. Grau-Campistany, ..., Y. Cajal. 2015. A bioinspired peptide scaffold with high antibiotic activity and low in vivo toxicity. *Sci. Rep.* 5:10558.
85. Xiong, M., M. W. Lee, ..., J. Cheng. 2015. Helical antimicrobial polypeptides with radial amphiphilicity. *Proc. Natl. Acad. Sci. USA*. 112:13155–13160.

**Biophysical Journal, Volume 111**

**Supplemental Information**

**Antimicrobial Peptides Share a Common Interaction Driven by Membrane Line Tension Reduction**

**J. Michael Henderson, Alan J. Waring, Frances Separovic, and Ka Yee C. Lee**

## Experimental Methods

### Peptide stocks

Peptide stocks at 1 mg/mL were generally prepared in a HEPES buffered saline (HBS) solution containing calcium (HBS+Ca: 10 mM HEPES, 150 mM NaCl, 2 mM Ca<sup>2+</sup>, pH 7.5). Given alamethicin's larger hydrophobicity as compared to other AMPs, alamethicin was first serially diluted from 5 to 1 mg/mL using a 50% (v/v) aqueous methanol solution. Poor solubility of caerin-1.3 and kalata-B3 was observed and instead were dissolved in HBS+Ca containing 5% DMSO to obtain transparent stocks at 1 mg/mL. Peptide concentration was quantified by UV absorbance using a Hewlett-Packard 8453 UV/Vis spectrophotometer, with calculated absorption coefficients of 1520 (PG-1), 3840 (human  $\beta$ -defensin-1), 5120 (histatin-2), and 27,500 (indolicidin) mol<sup>-1</sup> cm<sup>-1</sup>, respectively, at 280 nm. The stock concentrations of chromophoric lacking peptides were instead determined by the mass dissolved in a given volume and later found to have less than a 5.5% error from the desired concentration, as quantified by amino acid analysis at the W. M. Keck Foundation Biotechnology Resource Laboratory, Yale University, New Haven, CT.

### Preparation of large unilamellar vesicles

Large unilamellar vesicles (LUVs) were self-assembled via the freeze-thaw extrusion method (1). An aliquot of the dissolved lipid in chloroform was transferred to an acid-cleaned vial and a lipid film was formed on the glass walls with a stream of ultrahigh purity nitrogen gas (Airgas, Radnor Township, PA). The film was dried overnight under vacuum to ensure complete evaporation of the solvent. Ultrapure water was added to the dried lipid sample (achieving a typical concentration of 1 mg/mL) and multilamellar vesicles were formed by vigorous mechanical agitation for 1 hour at 40°C. After six freeze-thaw cycles, the lipid dispersion was extruded at least 21 times through polycarbonate membranes having a pore size of 100 nm (Avanti Polar Lipids, Alabaster, AL). The size distribution of the resulting LUVs was determined by dynamic light scattering (Zetasizer Nano-ZS, Malvern Instruments, Worcestershire, UK) and typically exhibited an average diameter of 130 ± 40 nm. LUVs were utilized within two weeks and stored in an incubator oven at 30°C to keep the vesicles above the main phase transition temperature for DMPC (T<sub>m</sub> = 24°C).

### Supported bilayer formation and atomic force microscopy

High grade mica (Ted Pella, Redding, CA) was fixed to a stainless steel specimen disc (Ted Pella, Redding, CA) and used as a solid substrate for supported phospholipid bilayer (SPB) formation. The mica was freshly cleaved and hydrated with a 10 mM MgCl<sub>2</sub> salt solution as divalent cations aid in the fusion of LUVs to negatively charged substrates (2, 3). Dilution of the LUV stock was made with the MgCl<sub>2</sub> solution to a concentration of 15 μg/mL, and 1 mL was injected into the imaging fluid cell. The solution was incubated for 3–5 minutes, during which bilayer patches self-assembled, covering approximately 20% of the mica surface in a given 20 x 20 μm<sup>2</sup> area. The superphase was exchanged for HBS+Ca to flush away un-fused vesicles.

Topographic images of the SPB patches were gathered in fluid at 30°C using a Cypher ES AFM (Asylum Research, Santa Barbara, CA) in tapping mode. Silicon-nitride cantilevers having a nominal spring constant of 0.25 N/m with sharpened silicon tips (Olympus BioLever Mini, BL-AC40TS, Asylum Research Probes, Santa Barbara, CA) were used and driven to a resonant



frequency (typically at 20 kHz) by blueDrive<sup>TM</sup> photothermal excitation. The tips were decontaminated by UV-generated ozone before an experiment (PSD-UV Surface Decontamination System, Novascan, Ames, IA). Given cantilever variability, the chosen setpoint fell between 80 and 95% of the free amplitude in our experiments, which corresponded to a deflection of 20–25 nm, ensuring ample sample clearance. To prevent membrane damage and image artifacts, the drive amplitude was adjusted to achieve an attractive imaging regime that minimized forces during scanning. Micrographs were obtained at a scan rate of 3.0 Hz with a resolution of 512 pixels/line. Peptide aliquots were prepared in HBS+Ca and following injection were incubated for at least 15 min before continuing imaging. Assuming the bilayer coverage is  $\sim 20\%$  of the  $1\text{ cm}^2$  mica substrate, the number of moles of deposited DMPC lipids and that of peptide can be easily estimated to calculate a peptide-to-lipid ( $P/L$ ) ratio. In the calculation, the area/molecule of DMPC was assumed to be  $60\text{ \AA}^2$  (4) and a volume of  $50\text{ }\mu\text{L}$  was used as a conservative estimate of the liquid droplet size based on the specifications of the Cypher ES AFM ([www.asylumresearch.com](http://www.asylumresearch.com)).

### Image processing and analysis

To improve image clarity, AFM scans were subjected to a first-order flattening procedure using the Asylum Research software implemented in IGOR Pro (WaveMetrics, Lake Oswego, OR) to compensate for sample tilt and offset between scan lines (raised features were excluded from the flattening algorithm). Similarly to Blanchette et al. (5), the bilayer shape factor,  $S$ , was calculated according to

$$S = P^2/4\pi A \quad (1)$$

to quantify membrane morphological changes as a result from AMP activity; here  $P$  is the perimeter and  $A$  is the surface area of the bilayer patch. Ideal circular morphologies will have a shape factor equal to 1, as derived from the perimeter and area equations for a circle. A given bilayer patch was selected by proper thresholding of the image to generate a mask, and then the perimeter length and surface area were calculated using the particle size analysis tool in Gwyddion (6). Any visible areas of mica substrate in perforated bilayers were excluded from the final mask, either through adjustment of the thresholding level and/or through the manual removal of mask pixels, so that the analysis was performed only on the membranes themselves. The bilayer height was analyzed from the distribution of surface heights over a scan (histogram analysis) or from a line section of a scan, depending on the quality of the image. As attractive mode imaging can artificially increase sample height profiles (7, 8) and lead to measurement variability between experiments, membrane height changes are reported as relative changes from the initial bilayer patch within an experiment.

### Calcein Leakage Assay.

The extent of vesicle leakage induced by the interaction of alamethicin was assessed from the de-quenching of the water-soluble, membrane impermeable dye, calcein (9–11). Calcein was purchased from Sigma-Aldrich (St. Louis, MO) as a disodium salt powder and used without further purification. Calcein-loaded DMPC vesicles were prepared by the extrusion method as previously explained in a solution containing 60 mM calcein and 10 mM HEPES at pH 7.5. The osmolality of the dye solution was approximately 391 mOsm (5005 OSMETTE II, Precision Systems, Natick, MA). Un-trapped calcein was separated from the vesicle suspension by size exclusion

chromatography (Superdex 75, 10 x 300 mm column, GE Healthcare) using an isotonic eluent (10 mM HEPES, 205 mM NaCl, pH 7.5) that was within 1–2 mOsm of the internal dye solution of the vesicles, made by the adjustment of the salt concentration. To ensure the vesicle suspension remained above the main phase transition temperature for DMPC ( $T_m = 24^\circ\text{C}$ ), the sample loop, eluent, tubing, and the column were maintained at a temperature between  $35^\circ\text{C}$ – $40^\circ\text{C}$  during gel filtration. The total lipid concentration of the collected vesicle fraction was determined by a phosphorous assay (12–14). Dye-loaded DMPC vesicles were utilized immediately for fluorescence measurements as they tended to leak their entire contents within a 24 hour period following preparation.

A quartz cuvette with a 1 cm pathlength was filled with 3 mL of a 135  $\mu\text{g}/\text{mL}$  solution of dye-loaded DMPC vesicles prepared in the isotonic buffer. Changes in the fluorescence intensity from the de-quenching of calcein were monitored at 515 nm at  $30^\circ\text{C}$  using a FluoroLog-3 spectrofluorometer (Horiba, Edison, NJ) with an excitation wavelength of 490 nm. The background fluorescence of the lipid sample alone,  $I_o$ , was obtained prior to the addition of peptide which defined the starting point, i.e. time zero, of the experiment. Serial dilutions were made from the 1 mg/mL alamethicin stock, as described in the main body of the text, using the isotonic buffer such that approximately 30–70  $\mu\text{L}$  aliquots could be added to the cuvette to obtain the desired bulk concentration. However, the largest bulk concentration investigated, 50  $\mu\text{M}$  alamethicin, required the addition of approximately 300  $\mu\text{L}$  of the stock. The sample was gently stirred using a magnetic stir bar through the course of the measurement to ensure sample homogeneity. Finally, 100  $\mu\text{L}$  of 10 % (v/v) Triton X-100 was added to each sample to completely solubilize the vesicles and release all the entrapped calcein to determine the maximal fluorescence,  $I_{max}$ . The fractional release of calcein at a given time point,  $F_t$ , was calculated according to

$$F_t = (I_t - I_o)/(I_{max} - I_o). \quad (2)$$

The kinetics of vesicle leakage in relation to antimicrobial peptide activity have been reasonably well described by multi-exponential functions (15–18). All leakage curves were fit in MATLAB (MathWorks Inc., Natick, MA) to a double-exponential decay model,

$$F_t = 1 - A_1e^{-t \cdot k_1} - A_2e^{-t \cdot k_2}, \quad (3)$$

where  $A_1$  and  $A_2(\equiv 1 - A_1)$  are the amplitudes, and  $k_1$  and  $k_2$  are the respective rate constants of the individual exponential functions that describe two distinct processes leading to calcein leakage. Given that the overall leakage can be dominated by process 2 ( $A_2 = 1$ ) in the limit when either  $A_1$  or  $k_1$  vanishes, process 2 can be attributed to pores whose probability to form increases with increasing peptide concentration. Therefore, process 1 refers to a graded-leakage mechanism as  $A_1$  can only approach finite values below 1. A graded-leakage mechanism has been explained by the asymmetric insertion of peptides into the outer leaflet of the membrane which causes transient defects to form that allow peptides to translocate across the membrane to establish a mass balance. These transient openings lead to a graded mechanism of dye leakage that has been observed with several other AMPs (17, 19–21). The apparent leakage rate,  $k_{app}$ , was calculated by an amplitude-weighted average according to

$$k_{app} = A_1k_1 + (1 - A_1)k_2, \quad (4)$$

as was similarly done by Gregory et al. (19, 20).

### **Dynamic Light Scattering**

To ascertain the effect that alamethicin has on the integrity of the vesicles, changes in the size distribution of the dye-loaded DMPC LUVs was monitored by dynamic light scattering (Zetasizer Nano-ZS, Malvern Instruments, Worcestershire, UK). Briefly, 3 mL of a 135  $\mu\text{g}/\text{mL}$  solution of dye-loaded DMPC vesicles was prepared as described above to which an appropriate amount of alamethicin was added to reach a desired bulk concentration. Approximately 1 mL of the mixed DMPC-alamethicin solution was added to fill a capillary cell for measurement. DLS measurements were performed at 30°C and the sample was illuminated with 633 nm light provided from a He-Ne laser. The scattered light from the sample was analyzed at an angle of 173° from the incident beam in the backscattering configuration. Correlation analysis gave the diffusion coefficients of the vesicles from which the diameters of the LUVs were calculated using the Stokes-Einstein relationship. Scattering data were gathered over 15 minutes in which 12 individual measurements were combined to generate a single run. Reproducibility was assessed across 3 separate runs and averaged.

**Table S1:** Characteristics of the investigated AMPs.

Peptide	Charge at pH 7.5	No. of Residues	Sequence
Dermcidin	-3	48	SSLLEKGLDGAKKAVGGLGKLGKDAVEDLESVGK-GAVHDVKDVLDSVL
Kalata-B3	-2	30	<div style="border: 1px solid black; padding: 2px; display: inline-block;">           GLPTCGETCFGGTCNTPGCTCDPWICTRD         </div> 
Caerin-1.3	0	25	GLLSVLGSVAQHVLPHVVPVIAEHL - NH <sub>2</sub>
Alamethicin	0	20	Ac-UPUAUAQUVUGLUPVUUQQ-Phl
Pardaxin-1	0	33	GFFALIPKIISSPLFKTLLSAVGSALSSSGEQE
Histatin-2	0	27	RKFHEKHSHSHREFPFYGDYGSNYLYDN
Aurein-1.1	+1	13	GLFDIIKKIAESI - NH <sub>2</sub>
Citropin-1.1	+2	16	GLFDVIKKVASVIGGL - NH <sub>2</sub>
Magainin-1	+3	23	GIGKFLHSAGKFGKAFVGEIMKS
Dermaseptin-1	+3	34	ALWKTMLKKLGTMLHAGKAALGAAADTISQGTQ
Indolicidin	+4	13	ILPWKWPWWPWR - NH <sub>2</sub>
Human $\beta$ -Defensin-1	+4	36	DHYNCVSSGGQCLYSACPIFTKIQTGTCYRGKAKCCK 
Protegrin-1	+7	18	RGGRLCYCRRRFCVGVGR - NH <sub>2</sub> 

The terminal protecting group abbreviations are Ac- for acetyl and NH<sub>2</sub> for carboxamide. The following abbreviations are used for non-standard residues: U,  $\alpha$ -aminoisobutyric acid; Phl, L-phenylalaninol. Solid lines indicate residue connections in cyclic structures while disulfide bonds between cysteine residues are indicated by dashed lines.



**Table S2:** Minimum inhibitory concentrations, MIC ( $\mu\text{M}$ ), of the investigated AMPs or related isoforms against susceptible Gram-negative and Gram-positive bacterial strains.

Peptide	Gram -		Gram +		Ref.
	<i>E. coli</i>	<i>P. aeruginosa</i>	<i>S. aureus</i>	<i>B. subtilis</i>	
Dermcidin	0.21 <sup>a</sup>	?	0.21 <sup>a</sup>	?	(22)
Kalata-B1*	>500	>500	>500	?	(23)
Caerin-1.1*	100–200 <sup>a,b</sup>	?	3 <sup>a</sup>	12 <sup>a</sup>	(24)
Alamethicin	8–102 <sup>a,c</sup>	?	18 <sup>a</sup>	8	(25–27)
Pardaxin-1	13	25	?	?	(28)
Aurein-1.2*	75	?	35 <sup>a</sup>	?	(29, 30)
Citropin-1.1	40–79 <sup>a,b</sup>	?	8 <sup>a</sup>	2 <sup>a</sup>	(24)
Magainin-2*	0.1–2 <sup>a,d</sup>	0.8–52 <sup>a,d</sup>	2–52 <sup>a,d</sup>	?	(31)
Dermaseptin-1	12	?	12	?	(32)
Indolicidin	0.3–4 <sup>a,d</sup>	4–67 <sup>a,d</sup>	2–17 <sup>a,d</sup>	?	(31)
Protegrin-1	0.35 <sup>a</sup>	0.23 <sup>a</sup>	0.79 <sup>a</sup>	6 <sup>a</sup>	(33, 34)

? MIC value could not be found.

\* Related isoform that differs by one amino acid residue to the investigated peptide in Table S1.

<sup>a</sup> MIC value(s) converted from results reported in  $\mu\text{g/mL}$ .

<sup>b</sup> Reported range from two strains.

<sup>c</sup> Reported range from two peptide isoforms.

<sup>d</sup> Reported range from 30 clinical isolates.

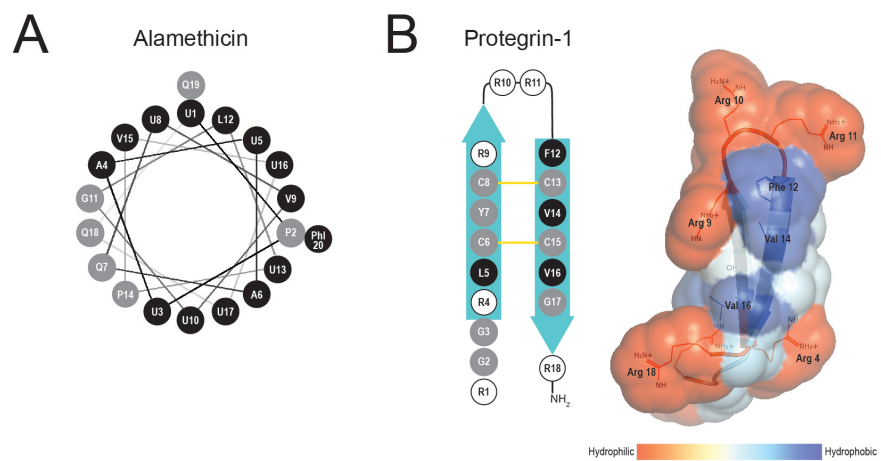


**Figure S1:** Secondary structure representation of alamethicin (A) and protegrin-1 (B). In the helical wheel diagram of alamethicin,  $\alpha$ -aminoisobutyric acid and L-phenylalaninol are abbreviated with U and Phl, respectively. The hydrophobicity of protegrin-1 (PDB ID: 1PG1) was rendered as a colored surface in PyMOL based on the Kyte-Doolittle scale (35), where the gradation of color from red to blue signifies a transition from more to less hydrophilic. Residues in the primary sequences were color-coded according to the following scheme: black, apolar; gray, polar un-charged; and white, charged. Disulfide bonds are represented as yellow lines between connected cysteine residues.



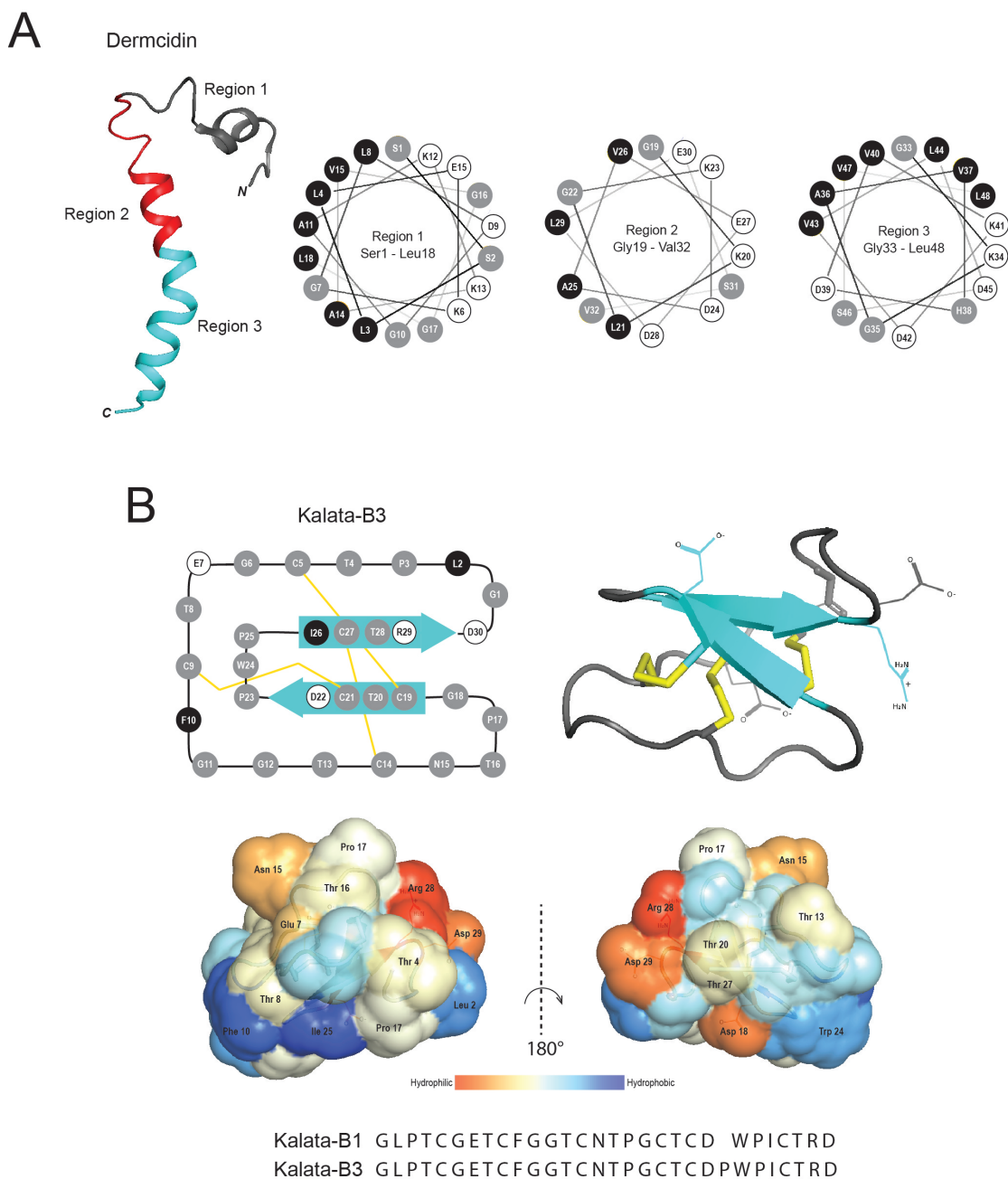


**Figure S3:** Secondary structure representations of the negatively charged AMPs, dermcidin (A) and kalata-B3 (B), featured in Fig. 4 of the main text. (A) The secondary structure of dermcidin (PDB ID: 2KSG) was rendered in PyMOL to display its flexible helix-hinge-helix type motif consisting of three amphiphilic helices colored black (region 1, Ser1–Leu18), red (region 2, Gly19–Val32), and cyan (region 3, Gly33–Leu48). Helical wheel diagrams were constructed for each region in order to show that an overall amphipathic structure can be formed when the helices are properly oriented with respect to one another. (B) Since no PDB file could be obtained for the cyclotide kalata-B3, we instead rendered kalata-B1 (PDB ID: 1ZNU) in PyMOL as it only differed from kalata-B3 by a lack of a single proline found in the C-terminal end. The hydrophobicity of kalata was rendered as a colored surface based on the Kyte-Doolittle scale (35), where the gradation of color from red to blue signifies a transition from more to less hydrophilic. Residues in the primary sequences were color-coded according to the following scheme: black, apolar; gray, polar un-charged; and white, charged. Disulfide bonds are represented as yellow lines between connected cysteine residues.

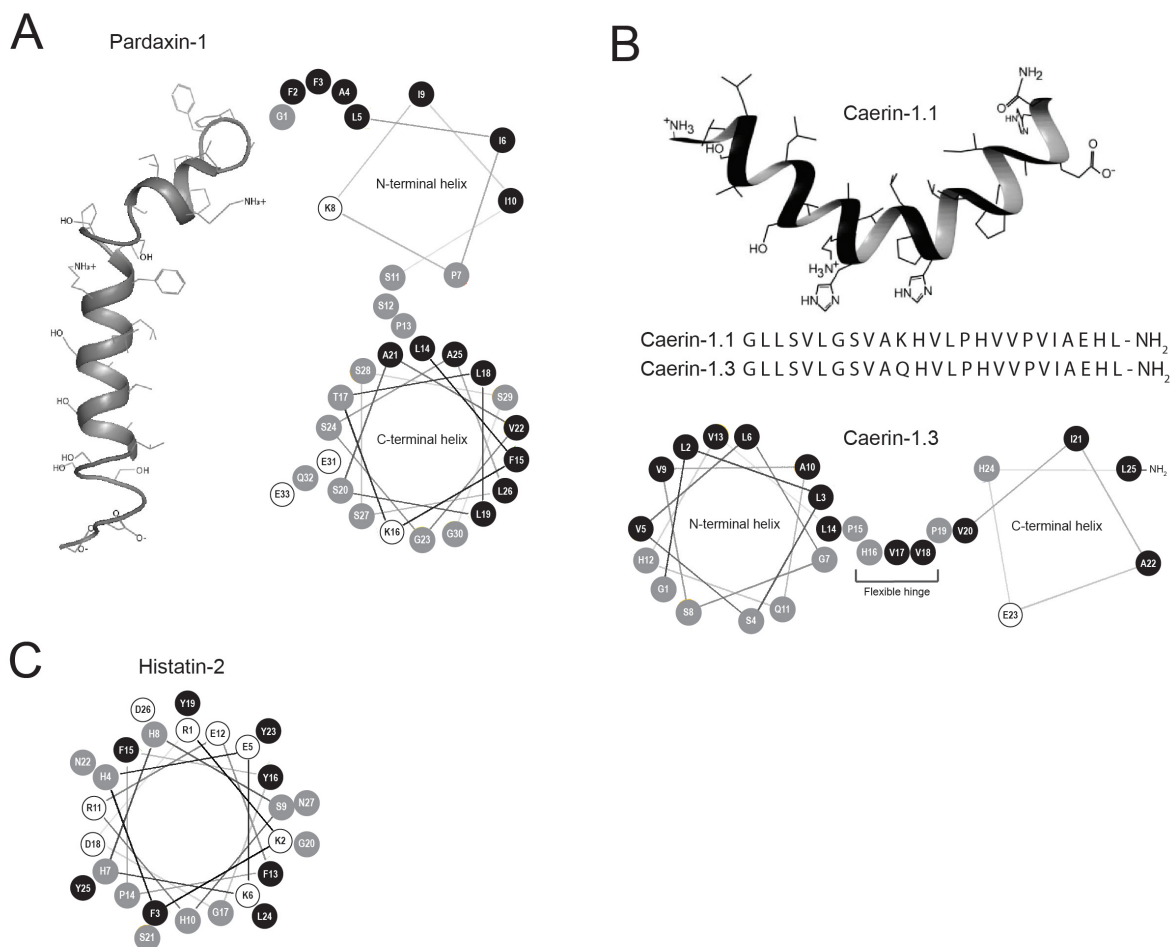


**Figure S4:** Secondary structure representations and helical wheel diagrams of the neutral AMPs, pardaxin-1 (A), caerin-1.3 (B), and histatin-2 (C), featured in Fig. 5 of the main text. (A) Since no PDB file was present for pardaxin-1, the helical structure of pardaxin-Pa4 (PDB ID: 1XC0) was used as a template with which Gly31 was mutated to a Glu to make the primary sequence identical to that of pardaxin-1. (B) As no PDB file could be found of a caerin peptide in the database, the helical structure depicted in B is that of caerin-1.1 (reprinted from (36)), a homolog of caerin-1.3 that differs by only one residue. (C) While limited structural information exists for histatin peptides, the helical wheel generated for histatin-2 shows no clear segregation of hydrophilic and hydrophobic residues that form an ideal amphipathic secondary structure. Residues in the primary sequences were color-coded according to the following scheme: black, apolar; gray, polar un-charged; and white, charged.



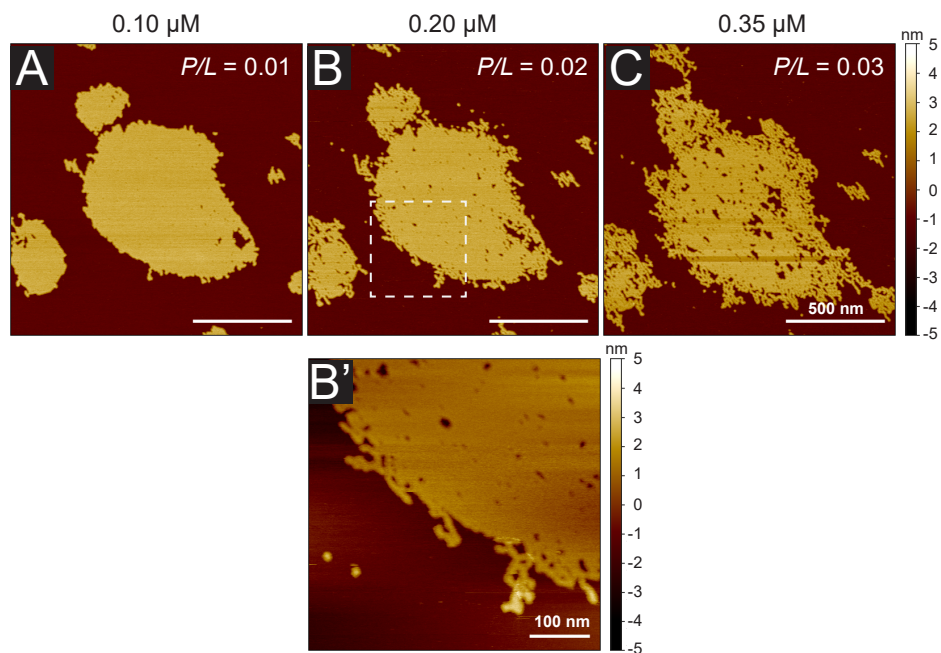


**Figure S5:** Membrane structural transformations induced by PG-1. The formation of porous defects within the bilayer core was observed at  $0.10 \mu\text{M}$  PG-1 (A) which increased in number and size in the range of  $0.20$  to  $0.35 \mu\text{M}$  PG-1 (B and C). The dashed box in B indicates a zoomed in region ( $500 \times 500 \text{ nm}^2$ ) that is shown in B'. All images were gathered at  $30^\circ\text{C}$ . White scale bars are  $500 \text{ nm}$ , unless otherwise indicated.

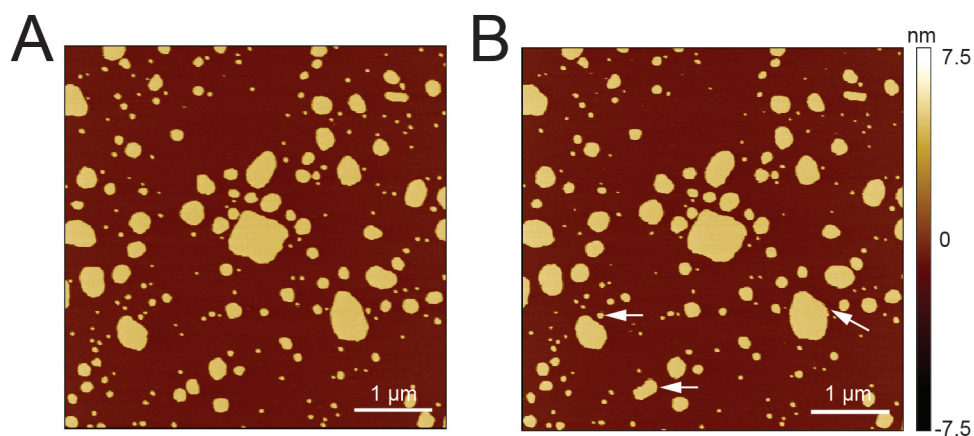


**Figure S6:** DMPC bilayers imaged under different buffered superphase conditions. (A) Prior to the introduction of alamethicin (see Fig. 2 main text), the same DMPC bilayers were imaged first in the HBS+Ca buffer ( $10 \text{ mM}$  HEPES,  $150 \text{ mM}$  NaCl,  $2 \text{ mM}$   $\text{Ca}^{2+}$ ,  $\text{pH}$   $7.5$ ) alone. (B) The superphase was then exchanged with a HBS+Ca solution containing  $2\%$  DMSO and  $4\%$  MeOH (v/v) to mimic that of a  $50 \mu\text{M}$  alamethicin injection. Negligible changes between (A) and (B) were observed and only three events of adjacent bilayer fusion were seen (white arrows) within the  $5 \times 5 \mu\text{m}^2$  viewing area. Images were gathered at  $30^\circ\text{C}$ . White scale bars are  $1 \mu\text{m}$ .

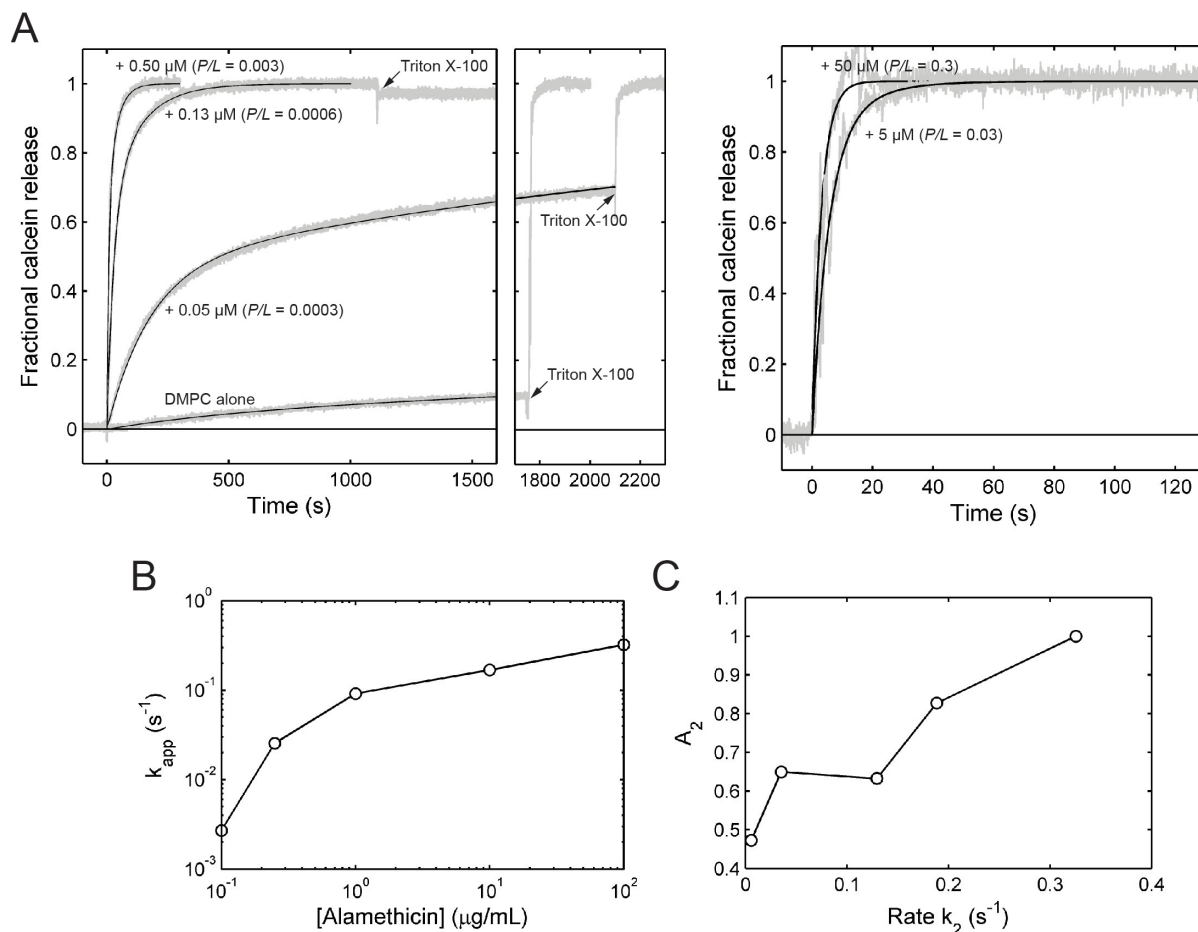
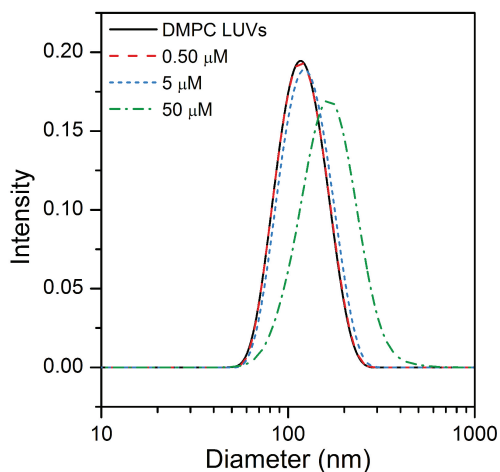


**Figure S7:** Concentration-dependent leakage of entrapped calcein in DMPC LUVs by alamethicin. For all experiments the total lipid concentration was held constant at  $135 \mu\text{g/mL}$  and the experimental temperature was maintained at  $30^\circ\text{C}$ . (A) Higher bulk concentrations of alamethicin resulted in progressively higher plateaus in the maximum fraction of released calcein in the leakage profiles. Complete leakage was eventually obtained at a bulk alamethicin concentration of  $0.13 \mu\text{M}$  and higher. Detergent addition to these samples would slightly dilute the free calcein by roughly 5% from a lowering of the fluorescence intensity; consequently, all the calcein had been released from the addition of alamethicin prior to the Triton X-100 addition. (B) As evident in the leakage profiles presented in A, the apparent rate of leakage,  $k_{app}$ , steadily increased with increasing alamethicin concentration, signifying more membrane-bound alamethicin to perturb the integrity of the calcein-loaded vesicles. (C) The resulting parameters  $A_2$  and  $k_2$  from the double-exponential fit to the leakage profiles were correlated to each other. As the bulk concentration of alamethicin was increased, the leakage process corresponding to stable pore formation (process 2 with amplitude  $A_2$ ) had a greater contribution (i.e., a greater weight or amplitude) to the overall leakage profile with a higher density of pores from the increase in  $k_2$ .



Sample	Average size ( $\pm$ s.d.)
DMPC LUVs	122.1 $\pm$ 32.9 nm
DMPC + 0.50 $\mu$ M alamethicin ( $P/L = 0.003$ )	122.5 $\pm$ 32.9 nm
DMPC + 5.0 $\mu$ M alamethicin ( $P/L = 0.03$ )	128.2 $\pm$ 35.5 nm
DMPC + 50 $\mu$ M alamethicin ( $P/L = 0.3$ )	173.0 $\pm$ 56.9 nm

**Figure S8:** DLS analysis of DMPC LUV size distribution changes at 30°C with increasing bulk concentrations of alamethicin.

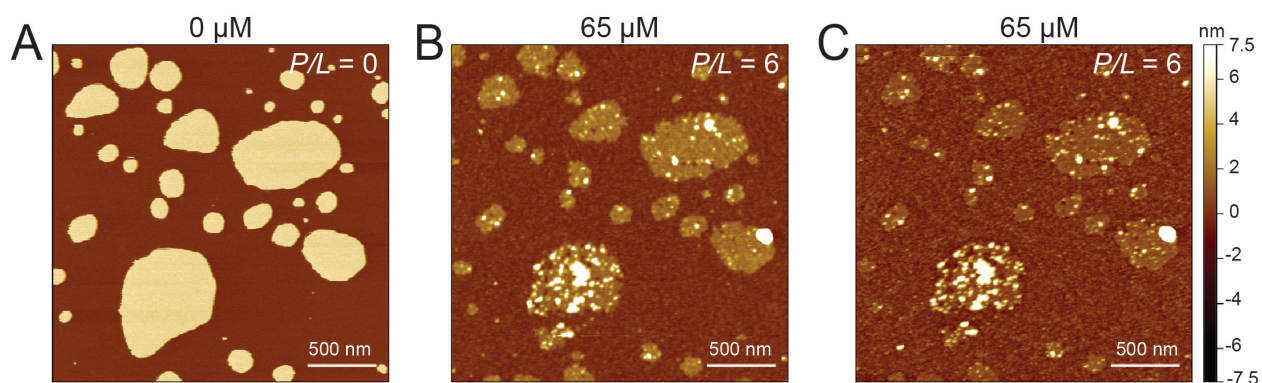


**Figure S9:** Time lapse imaging of kalata-B3's slow solubilization of zwitterionic DMPC bilayers. (A) DMPC bilayer patches in the absence of peptide. (B) Image collected 15 min following the addition of a 65  $\mu$ M aliquot of kalata-B3. (C) Image collected 1 hour later after B. All images were gathered at 30°C. White scale bars are 500 nm.

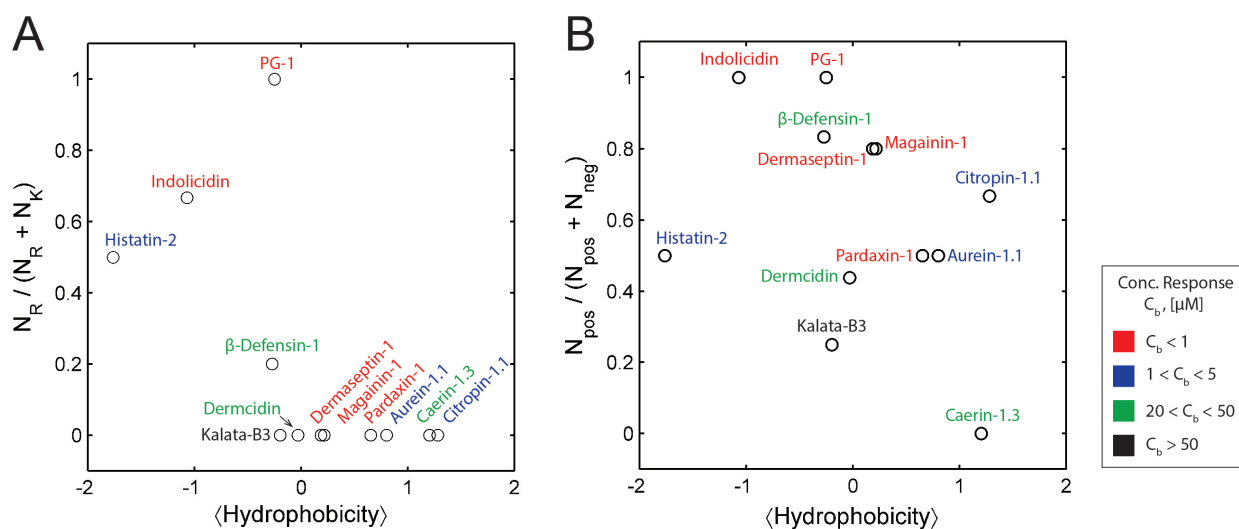


**Figure S10:** Amino acid content comparison of the investigated line-active peptides. (A) The ratio of the number of arginines to the number of arginines + number of lysines ( $N_R/(N_R+N_K)$ ) plotted against their average hydrophobicity (Kyte-Doolittle scale). (B) The ratio of the number of positive residues (arginines + lysines) to the total number of charged residues (positive + negative), ( $N_{pos}/(N_{pos}+N_{neg})$ ), plotted against the average hydrophobicity (Kyte-Doolittle scale) calculated for each peptide. The peptides were color-coded based upon their concentration response ( $C_b$ ) in achieving a final micellized state.

## References

1. Muresan, A. S., and K. Y. C. Lee. 2001. Shape evolution of lipid bilayer patches adsorbed on mica: an atomic force microscopy study. *J. Phys. Chem. B.* 105:852–855.
2. Reviakine, I., and A. Brisson. 2000. Formation of supported phospholipid bilayers from unilamellar vesicles investigated by atomic force microscopy. *Langmuir.* 16:1806–1815.
3. Seantier, B., and B. Kasemo. 2009. Influence of mono- and divalent ions on the formation of supported phospholipid bilayers via vesicle adsorption. *Langmuir.* 25:5767–5772.
4. Kučerka, N., Y. Liu, N. Chu, H. I. Petrache, S. Tristram-Nagle, and J. F. Nagle. 2005. Structure of fully hydrated fluid phase DMPC and DLPC lipid bilayers using x-ray scattering from oriented multilamellar arrays and from unilamellar vesicles. *Biophys. J.* 88:2626–2637.
5. Blanchette, C. D., C. A. Orme, T. V. Ratto, and M. L. Longo. 2007. Quantifying growth of symmetric and asymmetric lipid bilayer domains. *Langmuir.* 24:1219–1224.
6. Nečas, D., and P. Klapetek. 2012. Gwyddion: an open-source software for SPM data analysis. *Cent. Eur. J. Phys.* 10:181–188.
7. R. Brandsch, G. B., and M.-H. Whangbo. 1997. On the factors affecting the contrast of height and phase images in tapping mode atomic force microscopy. *Langmuir.* 13:6349–6353.
8. San Paulo, A., and R. García. 2000. High-resolution imaging of antibodies by tapping-mode atomic force microscopy: attractive and repulsive tip-sample interaction regimes. *Biophys. J.* 78:1599–1605.
9. Allen, T. M., and L. G. Cleland. 1980. Serum-induced leakage of liposome contents. *BBA - Biomembranes.* 597:418 – 426.
10. Matsuzaki, K., M. Harada, T. Handa, S. Funakoshi, N. Fujii, H. Yajima, and K. Miyajima. 1989. Magainin 1-induced leakage of entrapped calcein out of negatively-charged lipid vesicles. *BBA - Biomembranes.* 981:130–134.
11. Pouny, Y., D. Rapaport, A. Mor, P. Nicolas, and Y. Shai. 1992. Interaction of antimicrobial dermaseptin and its fluorescently labeled analogs with phospholipid membranes. *Biochemistry.* 31:12416–12423.
12. Chen, P. S., T. Y. Toribara, and H. Warner. 1956. Microdetermination of phosphorus. *Anal. Chem.* 28:1756–1758.
13. Bartlett, G. R.. 1959. Phosphorus assay in column chromatography. *J. Biol. Chem.* 234:466–468.
14. Morrison, W.. 1964. A fast, simple and reliable method for the microdetermination of phosphorus in biological materials. *Anal. Biochem.* 7:218 – 224.
15. Arbuzova, A., and G. Schwarz. 1996. Pore kinetics of mastoparan peptides in large unilamellar lipid vesicles. *Progr. Colloid Polym. Sci.* 100:345–350.
16. Rex, S., and G. Schwarz. 1998. Quantitative studies on the melittin-induced leakage mechanism of lipid vesicles. *Biochemistry.* 37:2336–2345.
17. Heerklotz, H., and J. Seelig. 2007. Leakage and lysis of lipid membranes induced by the lipopeptide surfactin. *Euro. Biophys. J.* 36:305–314.
18. Andersson, A., J. Danielsson, A. Gräslund, and L. Måler. 2007. Kinetic models for peptide-induced leakage from vesicles and cells. *Euro. Biophys. J.* 36:621–635.
19. Gregory, S. M., A. Cavanaugh, V. Journigan, A. Pokorny, and P. F. Almeida. 2008. A quantitative model for the all-or-none permeabilization of phospholipid vesicles by the antimicrobial peptide cecropin A. *Biophys. J.* 94:1667–1680.



20. Gregory, S. M., A. Pokorny, and P. F. Almeida. 2009. Magainin 2 revisited: a test of the quantitative model for the all-or-none permeabilization of phospholipid vesicles. *Biophys. J.* 96:116–131.
21. Heerklotz, H.. 2001. Membrane stress and permeabilization induced by asymmetric incorporation of compounds. *Biophys. J.* 81:184–195.
22. Schitteck, B., R. Hipfel, B. Sauer, J. Bauer, H. Kalbacher, S. Stevanovic, M. Schirle, K. Schroeder, N. Blin, F. Meier, G. Rassner, and C. Garbe. 2001. Dermcidin: a novel human antibiotic peptide secreted by sweat glands. *Nat. Immunol.* 2:1133–1137.
23. Tam, J. P., Y.-A. Lu, J.-L. Yang, and K.-W. Chiu. 1999. An unusual structural motif of antimicrobial peptides containing end-to-end macrocycle and cystine-knot disulfides. *Proc. Natl. Acad. Sci. U.S.A.* 96:8913–8918.
24. Brian Chia, C. S., Y. Gong, J. H. Bowie, J. Zuegg, and M. A. Cooper. 2011. Membrane binding and perturbation studies of the antimicrobial peptides caerin, citropin, and maculatin. *Biopolymers.* 96:147–157.
25. Wenschuh, H., M. Beyermann, H. Haber, J. K. Seydel, E. Krause, and M. Bienert. 1995. Step-wise automated solid phase synthesis of naturally occurring peptaibols using Fmoc amino acid fluorides. *J. Org. Chem.* 60:405–410.
26. Ayers, S., B. M. Ehrmann, A. F. Adcock, D. J. Kroll, E. J. Carcache de Blanco, Q. Shen, S. M. Swanson, J. O. Falkinham III, M. C. Wani, S. M. Mitchell, C. J. Pearce, and N. H. Oberlies. 2012. Peptaibols from two unidentified fungi of the order Hypocreales with cytotoxic, antibiotic, and anthelmintic activities. *J. Pept. Sci.* 18:500–510.
27. Barns, K. J., and J. C. Weisshaar. 2016. Single-cell, time-resolved study of the effects of the antimicrobial peptide alamethicin on *Bacillus subtilis*. *BBA-Biomembranes.* 1858:725–732.
28. Oren, Z., and Y. Shai. 1996. A class of highly potent antibacterial peptides derived from pardaxin, a pore-forming peptide isolated from Moses sole fish *Pardachirus marmoratus*. *Eur. J. Biochem.* 237:303–310.
29. Li, X., Y. Li, A. Peterkofsky, and G. Wang. 2006. NMR studies of aurein 1.2 analogs. *BBA-Biomembranes.* 1758:1203–1214.
30. Rozek, T., K. L. Wegener, J. H. Bowie, I. N. Olver, J. A. Carver, J. C. Wallace, and M. J. Tyler. 2000. The antibiotic and anticancer active aurein peptides from the Australian Bell Frogs *Litoria aurea* and *Litoria raniformis*. *Eur. J. Biochem.* 267:5330–5341.
31. Giacometti, A., O. Cirioni, F. Barchiesi, M. S. Del Prete, M. Fortuna, F. Caselli, and G. Scalise. 2000. In vitro susceptibility tests for cationic peptides: comparison of broth microdilution methods for bacteria that grow aerobically. *Antimicrob. Agents Chemother.* 44:1694–1696.
32. Savoia, D., R. Guerrini, E. Marzola, and S. Salvadori. 2008. Synthesis and antimicrobial activity of dermaseptin S1 analogues. *Bioorg. Med.* 16:8205–8209.
33. Steinberg, D. A., M. A. Hurst, C. A. Fujii, A. H. C. Kung, J. F. Ho, F. Cheng, D. J. Loury, and J. C. Fiddes. 1997. Protegrin-1: a broad-spectrum, rapidly microbicidal peptide with in vivo activity. *Antimicrob. Agents Chemother.* 41:1738–1742.
34. Lai, J. R., R. F. Epand, B. Weisblum, R. M. Epand, and S. H. Gellman. 2006. Roles of salt and conformation in the biological and physicochemical behavior of protegrin-1 and designed analogues: correlation of antimicrobial, hemolytic, and lipid bilayer-perturbing activities. *Biochemistry.* 45:15718–15730.
35. Kyte, J., and R. F. Doolittle. 1982. A simple method for displaying the hydropathic character of a protein. *J. Mol. Biol.* 157:105–132.

36. Pukala, T. L., J. H. Bowie, V. M. Maselli, I. F. Musgrave, and M. J. Tyler. 2006. Host-defence peptides from the glandular secretions of amphibians: structure and activity. *Nat. Prod. Rep.* 23:368–393.